SARS-CoV-2 nucleocapsid protein inhibits the PKR-mediated integrated stress response through RNA-binding domain N2b

Chiara Aloise, Jelle G. Schipper, Arno van Vliet, Judith Oymans, Tim Donselaar, Daniel L. Hurdiss,

Raoul J. de Groot* and Frank J.M. van Kuppeveld*

Virology Division, Department of Biomolecular Health Sciences, Faculty of Veterinary Medicine, Utrecht University, 3584 CL Utrecht, the Netherlands.

* These authors share senior authorship.

Address correspondence to Raoul de Groot (R.J.deGroot@uu.nl) or Frank van Kuppeveld (F.J.M.vanKuppeveld@uu.nl)

ABSTRACT

The nucleocapsid protein N of severe acute respiratory syndrome coronavirus 2 (SARS-CoV-2) enwraps and condenses the viral genome for packaging but is also an antagonist of the innate antiviral defense. It suppresses the integrated stress response (ISR), purportedly by interacting with stress granule (SG) assembly factors G3BP1 and 2, and inhibits type I interferon responses. To elucidate its mode of action, we systematically deleted and over-expressed distinct regions and domains. We show that N via domain N2b blocks PKR-mediated ISR activation, as measured by suppression of ISR-induced translational arrest and SG formation. N2b mutations that prevent dsRNA binding abrogate these activities also when introduced in the intact N protein. Substitutions reported to block post-translation modifications of N or its interaction with G3BP1/2 did not have a detectable additive effect. In an encephalomyocarditis virus-based infection model, N2b - but not a derivative defective in RNA binding - prevented PKR activation, inhibited β-interferon expression and promoted virus replication. Apparently, SARS-CoV-2 N inhibits innate immunity by sequestering dsRNA to prevent activation of PKR and RIG-I-like receptors. Similar observations were made for the N protein of human coronavirus 229E, suggesting that this may be a general trait conserved among members of other orthocoronavirus (sub)genera.

39 **SIGNIFICANCE STATEMENT**

40 SARS-CoV-2 nucleocapsid protein N is an antagonist of innate immunity but how it averts
41 virus detection by intracellular sensors remains subject to debate. We provide evidence that
42 SARS-CoV-2 N, by sequestering dsRNA through domain N2b, prevents PKR-mediated
43 activation of the integrated stress response as well as detection by RIG-I-like receptors and
44 ensuing type I interferon expression. This function, conserved in human coronavirus 229E, is
45 not affected by mutations that prevent posttranslational modifications, previously
46 implicated in immune evasion, or that target its binding to stress granule scaffold proteins.
47 Our findings further our understanding of how SARS-CoV-2 evades innate immunity, how
48 this may drive viral evolution and why increased N expression may have been a selective
49 advantage to SARS-CoV-2 variants of concern.

50 **INTRODUCTION**

51 Vertebrate cells are provided with a diversity of interconnected sensors and effectors to
52 timely detect and counter viral infection. Particularly dsRNA, an inevitable product of RNA
53 and DNA virus replication, triggers a vigorous intracellular antiviral response (1). For
54 example, binding of dsRNA by 2'-5'oligoadenylate (2-5A) synthase (OAS) leads to enzyme
55 activation and production of 2-5A, which in turn activates RNase L to stall the synthesis of
56 viral proteins through non-specific RNA degradation (2-7). Another dsRNA-activated
57 pathway, the integrated stress response (ISR) with proteinase kinase R (PKR) as key sensor,
58 entails inhibition of translation initiation and ultimately cell death. Upon dsRNA binding, PKR
59 dimerizes, autophosphorylates and then proceeds to phosphorylate the alpha subunit of
60 eukaryotic initiation factor eIF2, turning it into competitive inhibitor of guanine nucleotide
61 exchange factor eIF2b. In consequence, the production of eIF2-GTP-(Met)tRNA$_i^{Met}$ ternary
62 complex is downregulated, recognition of the initiation codon is blocked and cap-dependent
63 translation-initiation prevented (8-11). Polysome dissociation, ensuing activation of the
64 stress response, results in an excess of stalled 48S preinitiation complexes, which are stored
65 in cytoplasmic membraneless organelles called stress granules (SGs) (12-14).

66 SGs are dynamic ribonucleoprotein assemblies that are formed through liquid-liquid
67 phase separation with RNA binding protein Ras GTPase-activating protein-binding proteins 1
68 and 2 (G3BP1 and -2) functioning both as a molecular switches and main protein scaffolds
69 together with T-cell-restricted intracellular antigen 1 (TIA1) and TIA1-related protein (TIAR)
70 (15-19). The SGs thus serve as deposits from which mRNAs, poised for translation through
71 association with critical components of the translation machinery (40S ribosomal subunits,
72 eIF4E, eIF4G, eIF4A, eIF4B, Poly(A) binding protein, eIF3, and eIF2), can be rapidly retrieved.
73 SGs, however, are also considered a coordinating hub for the activation of other antiviral
74 defense mechanisms like those of RIG-I-like receptors (RLRs). Indeed, RIG-I and MDA5, RLR-
75 regulating PKR-activating protein (PACT), RLR-modulating ubiquitin ligases TRIM25 and
76 TRAF2, and polyubiquitin chains are all recruited to ISR-induced SGs (20-23).

77 The antiviral mechanisms elicited by dsRNA are highly effective, even to such an extent
78 that all known mammalian viruses code for one or more antagonists (11). Coronaviruses,
79 positive-stranded RNA viruses of exceptional genetic complexity, code for a universally
80 conserved endonuclease (EndoU) that efficiently prevents simultaneous activation of host
81 cell dsRNA sensors OAS, PKR and MDA5 through dsRNA decay (24-26). Illustrating the

82 importance of EndoU, mutants defective for EndoU are severely attenuated *in vivo*, and their
83 replication in cultured primary macrophages is restricted presumably due to high basal
84 expression levels of host sensors in these cells (25). EndoU is derived by proteolytic
85 processing of a large replicase polyprotein pp1ab, translated from the incoming viral
86 genome, and essential to evade early innate and intrinsic antiviral host cell responses.
87 Apparently, however, EndoU may not be sufficient to suppress dsRNA-mediated antiviral
88 activities during later stages of the viral life cycle. To express the open reading frames (ORFs)
89 downstream of the replicase gene, CoVs produce a 3' co-terminal nested set of subgenomic
90 mRNAs from which the structural proteins are translated in addition to a variety of so-called
91 accessory non-structural proteins. Some of the latter also have been shown to counteract
92 dsRNA-mediated antiviral host responses. For example, the ns4a protein of Middle East
93 Respiratory Syndrome coronavirus (MERS-CoV) prevents PKR-mediated stress by
94 sequestering dsRNA (27, 28), whereas the MERS-CoV ns4b protein is a phosphodiesterase
95 (PDE) and antagonizes the OAS-RNase L pathway by enzymatically degrading 2-5A activators
96 (29). Non-related PDEs, ns2 proteins, are found in members of the subgenus *Embecovirus*,
97 including human coronavirus OC43 (30). Finally, a specific inhibitor of the ISR was found in
98 gammacoronaviruses of cetaceans. The beluga whale coronavirus accessory protein 10
99 (BWCoV acP10) blocks p-eIF2-eIF2B association to allow continued formation of the ternary
100 complex and unabated global translation even at high p-eIF2 levels that would otherwise
101 cause translational arrest (31).
102 Apparently, CoVs rely on redundancy in antagonists and antagonistic mechanisms to
103 effectively counter dsRNA-induced antiviral host responses. Likewise, the current pandemic
104 severe acute respiratory syndrome coronavirus 2 (SARS-CoV-2) codes for an ISR inhibitor
105 additional to EndoU (32). Its nucleocapsid protein (N) was reported to block the ISR and to
106 inhibit SG formation in a PKR- and G3BP1-dependent fashion (33-36). In apparent
107 concordance, proteomics studies and structural analyses provided evidence for physical
108 interactions between N and the SG key components G3BP1 and G3BP2 (33, 37-40).
109 Coronavirus N proteins have a modular structure with N-terminal and C-terminal RNA-
110 binding domains, called N1b and N2b respectively, bounded by largely disordered regions.
111 Here, we took a reductionistic approach involving systematic deletion and individual
112 transient expression of the different regions and domains. We show that the N2b domain is
113 critical and sufficient to counter the ISR. Single site mutations in N2b that block dsRNA

114 binding prevent PKR activation. This activity is not affected by posttranslational
115 modifications elsewhere in the N protein that are known to regulate RNA binding nor
116 dependent on physical interaction with G3BP1 and G2BP2. Using the encephalomyocarditis
117 virus as a surrogate infection system we show that N2b domain prevents PKR-mediated
118 activation of the ISR and suppresses IFNβ expression also in virus-infected cells. Our findings
119 suggest that in addition to a function in replication and genome packaging, SARS-CoV-2 N
120 functions as a classical antagonist of dsRNA-induced host defense.
121

122 **RESULTS**

123 **SARS-CoV-2 N inhibits PKR-induced ISR.** Transfection of cells with specific expression
124 plasmids like pEGFP-N3 triggers the ISR through dsRNA-mediated PKR activation, resulting in
125 translation arrest and the formation of SGs (Fig. 1A) (27, 41-43). This phenomenon allows for
126 a convenient method to identify potential viral ISR antagonists by transiently expressing
127 these proteins genetically fused to enhanced green fluorescent protein (EGFP) (27, 31). The
128 expression levels of these fusion proteins, as judged by fluorescence microscopy, can then
129 be compared to that of EGFP alone as an indicator for translation arrest and the prevention
130 thereof. In addition, SG formation can be assessed by immunofluorescence analysis (IFA) by
131 staining the transfected cells for established SG markers like G3BPs or eIF3. This procedure
132 previously allowed us to identify several stress antagonists including MERS-CoV 4a and
133 Beluga whale coronavirus AcP10 (27, 31).

134 SARS-CoV-2-infected Vero E6-TMPRRS2 cells, identified by detection of dsRNA, were virtually
135 devoid of SGs, suggestive of virus-induced suppression of the ISR (Fig. S1). While probing
136 SARS-CoV-2 proteins for a potential role in ISR inhibition, we noted that in transfected
137 wildtype (wt) HeLa cells, the expression levels of the SARS-CoV-2 N-EGFP fusion protein were
138 strongly increased as compared to the EGFP control. This pattern of enhanced expression in
139 a sizeable population of transfected cells was similar to that observed for established ISR
140 antagonists (Fig. 1B). Moreover, like these antagonists, SARS-CoV-2 N significantly reduced
141 the number of transfected cells with stress granules both in wildtype HeLa (HeLa wt) as well
142 as in A549 cultures (Fig. 1B). SG suppression was observed also in cells with fluorescence
143 intensities just above the background, suggesting that low levels of N-EGFP are already
144 sufficient to prevent SGs to form.

145 To confirm that expression of EGFP was suppressed due to PKR-induced ISR-mediated
146 translational arrest, we repeated the experiments in PKR-deficient HeLa PKR^{KO} cells. Indeed,
147 EGFP expression was increased and SGs were absent in these cells (Fig. 1C). In further
148 accordance, PKR was activated -as indicated by PKR phosphorylation- in HeLa wt cells
149 expressing EGFP but not in cells expressing EGFP-N. (Fig. 1D, left panel). Finally, Western blot
150 analysis confirmed that EGFP-N was expressed to similar levels in HeLa wt and PKR^{KO} cells.
151 Levels of EGFP, however, were strongly increased (about 7-fold) in HeLa PKR^{KO} cells (Fig. 1D,
152 right panel). The combined findings identify SARS-CoV-2 N as an ISR antagonist that prevents
153 translational arrest and ensuing SG formation by acting as a PKR inhibitor.

154 The N protein of another betacoronavirus, MERS-CoV, was previously noted to suppress
155 SG formation too (35). Interestingly, we observed inhibition of translational arrest and SG
156 formation also in cells expressing the N protein of human alphacoronavirus 229E (HCoV-
157 229E) (Fig. 1E). Apparently, N-mediated suppression of the ISR is not unique to
158 betacoronaviruses but may well be a general trait conserved among members of other
159 orthocoronavirus (sub)genera.
160
161 **Domain N2b is essential and sufficient for suppression of PKR-induced SG formation.** The N
162 proteins from the four CoV genera share only 27 to 30% sequence identity but are conserved
163 in their modular organization (Fig. 2A) ((44, 45) for a review see (46)). They are comprised of
164 two ordered domains, the N-terminal domain (N1b also called NTD) and the C-terminal
165 domain (N2b aka CTD) (in SARS-CoV-2 N, residues 49-175 and 248-365, respectively). N1b
166 and N2b are separated and flanked by segments, predicted to be at least partially disordered
167 (N1a, N2a and N3). N1b and N2b have been implicated in RNA binding and, in case of N2b,
168 also in N dimerization. Indeed, in infected cells and upon heterologous expression, CoV N
169 proteins form homodimers that, in turn, assemble into tetramers mediated by N3 (47). The
170 N2a central spacer contains a serine- and arginine-rich (SR) region, immediately downstream
171 of N1b, the regulated phosphorylation of which is deemed important for N function during
172 different stages of the CoV replication cycle (48-50). The primary function of N is in virus
173 assembly. It condenses newly produced gRNA into helical nucleocapsids, apparently with
174 N2b controlling target selectivity (51, 52), and then drives envelopment by binding to the
175 viral membrane protein M via N3. However, N has several functions auxiliary to virion
176 morphogenesis. At the very start of the infectious cycle, N is essential for the initiation of
177 infection by the incoming gRNA through association of SR with the cytosol-exposed
178 ubiquitin1 domain of replication organelle pore protein nsP3 (50, 53). Moreover,
179 purportedly relevant to ISR suppression, N binds to G3BP1 and 2 through segment N1a (38,
180 40, 54).
181 To determine the molecular basis for ISR suppression, we constructed a library of N
182 mutants with partially disordered regions and domains either systematically deleted or
183 expressed in isolation. As shown in Fig. 2, suppression was lost upon deletion of subdomain
184 N2b. Moreover, expression of N2b in isolation caused a reduction in SGs to an extent similar

185 to that of full-length N. The data therefore suggested that ISR inhibition and SG suppression
186 as observed for the intact N protein is mediated at least in part by N2b.
187
188 **N2b mutations that disrupt dsRNA binding abrogate suppression of SG formation.** N2b
189 binds both single and double stranded oligonucleotides, whether RNA or DNA (46, 55, 56).
190 Hence, a possible mechanism for N2b to prevent PKR-induced activation of the ISR is by
191 sequestering dsRNA. Crystal structural analysis revealed that N2b homodimers form a
192 rectangular slab with wide faces of 45 Å × 35 Å in dimension (55). One is comprised of an
193 interlaced inter-molecular four-stranded β-sheet and predominantly negatively charged, the
194 other of two α-helical regions separated by a shallow central, positively charged groove
195 thought to be the oligonucleotide binding site (46, 55, 57, 58). Within the groove, there are
196 several conserved positively charged residues with their surface-exposed side chains
197 seemingly poised for interaction with nucleic acid, in particularly Lys^{257} and Lys^{261} (**Fig. 3A**).
198 The binding by bacterially-expressed N2b of synthetic RNA oligonucleotides, whether single
199 or double-stranded, SARS-CoV-2 derived (highly conserved 3' UTR stem-loop II motif, s2m;
200 (59)) or a scrambled version thereof, can be readily demonstrated by electrophoretic
201 mobility assay (EMSA) (**Fig. 3A**, **B**).
202 To test whether Lys^{257} and Lys^{261} are involved in RNA binding and whether such binding is
203 important to counteract the ISR and suppress SG formation, they were replaced by Ala,
204 separately and in combination. Indeed, dsRNA binding was either significantly reduced or
205 lost beyond detection upon substitution of Lys^{257} and Lys^{261}, respectively (**Fig. 3B**). In
206 accordance, upon Ala substitution of Lys^{261} or Lys^{257}, the mutant N2b proteins no longer
207 rescued protein synthesis (**Fig. 3C**) and lost their capacity to suppress the formation of SGs,
208 either completely (Lys^{261}) or partially (Lys^{257}) (**Fig. 3D**). Notably, Ala substitution of other
209 surface-exposed charged residues (Gln^{272}, Gln^{289}, Arg^{276}, Arg^{293}), not located within the RNA
210 binding groove but rather implicated in N2b inter-dimer association (46, 56), did not
211 detectably affect SG formation (**Fig. 3D**).
212 Importantly, also in the intact N protein, Lys^{261}Ala substitution abrogated inhibition of
213 translational arrest as well as SG formation and so did the Lys^{257}Ala mutation (**Fig. 3C**, **D**). It is
214 unknown why the latter mutation exerts a stronger effect in the context of the full-length
215 protein than in N2b. The combined data, however, do show that Lys^{261} and Lys^{257} are
216 required for nucleic acid binding by N2b and suggest that this capacity to bind RNA is

217 essential for SG suppression. Moreover, the observation that also for the intact N protein SG
218 suppression was reduced to background levels by single site Lys^{261}Ala and Lys^{257}Ala
219 substitutions suggests that inhibition of PKR-induced ISR by SARS-CoV-2 N critically relies on
220 N2b and N2b-mediated RNA binding. Notably, the N protein of alphacoronavirus HCoV-229E
221 also lost its capacity to block SG formation when the orthologous N2b residues, Lys^{246} and
222 Lys^{250}, were substituted (**Fig. 3C, D**), suggestive of a common mechanism for ISR inhibition
223 through the binding of RNA.
224
225 **N2b-mediated inhibition of PKR-induced SG formation is not affected by posttranslational**
226 **modifications of N.** Previous studies identified N as a multifunctional protein involved in
227 different aspects of the viral replication cycle beyond viral assembly. Its activity apparently is
228 regulated by posttranscriptional modifications such as differential phosphorylation of the SR
229 domain, which alters RNA binding affinity (60, 61), and acetylation at Lys^{375}, reportedly
230 essential for liquid–liquid phase separation of N-RNA ribonucleoprotein complexes (62).
231 Arginine methylation of SARS-CoV-2 nucleocapsid protein at Arg^{95} and Arg^{177} was reported
232 to regulate RNA binding and its ability to suppress stress granule formation (33).
233 To test the importance of these posttranscriptional modifications on N2b-mediated
234 inhibition of SG formation, we performed site-directed mutagenesis in the context of the
235 intact N protein. Suppression of SG formation was not affected by Ala substitution of Arg^{95}or
236 Lys^{375} indicating that methylation and acetylation of N is not essential (**Fig. 4A**, **B**).
237 An N derivative in which phosphorylation of the SR segment was prevented through Ala
238 substitution of 13 out of 14 Ser residues (13S>A) displayed a cellular distribution distinctively
239 different from that of the parental wildtype protein, accumulating in large aggregates
240 enriched for G3BP1 but mostly devoid of eIF3 (**Fig. 4A**; **Fig. S3**). These deposits differed in
241 size, appearance and composition from typical SG. Importantly, the expression levels of the
242 N-13S>A mutant were like those of wildtype N, as judged by fluorescence intensity observed
243 in IFA, and consistently higher than those of EGFP (**Fig. 4A**). We interpret the findings to
244 indicate that the SR mutations may cause the N protein to aggregate but do not affect
245 inhibition of ISR-induced translational arrest. The results confirm those of our systematic
246 deletion analysis (Fig. 2).
247

248 **N2b-mediated inhibition of SG formation is not affected by disruption of the G3BP binding**
249 **motif.** A ΦxFG motif within N1a (residues 15-18), required for association with G3BP1 and 2
250 (40), was recently proposed to rewire the G3BP interactome to disrupt stress granules (38).
251 To investigate a possible role of N-G3BP interaction in suppressing PKR-induced SGs, we
252 mutated the N1a ΦxFG motif through Ala substitution of key residue Phe^{17} (mut 1A) or by a
253 combination of Ala substitions: Arg^{14} and Ile^{15} (mut 2A), Ile^{15}, Phe^{17} and Gly^{18} (mut 3A), or
254 Ile^{15}, Thr^{16}, Phe^{17} and Gly^{18} (mut 4A). In each case, binding to endogenous G3BP1 was no
255 longer detectable by pull down assay (Fig. 4C) yet suppression of SG formation was not
256 affected (Fig. 4A, B). Conversely, N proteins with N2b mutations to abrogate dsRNA binding
257 no longer blocked the ISR (Figs. 3 and 4B, C) nor inhibited SG formation, even though N1a
258 was still intact to bind G3BP1 to similar extent as wildtype N (Fig. 4C). Note that for these
259 N2b mutants N-G3BP association could not readily be assessed in HeLa wt cells. As a result of
260 PKR-activation (Fig. 4C) and ISR-mediated translational arrest, their expression levels were
261 strongly reduced as compared to those of wt N and the amounts of coprecipitated G3BP1
262 were below the detection level of our Western blot analysis. Unperturbed G3BP binding,
263 however, was evident, when assessed in HeLa PKR^{KO} cells (lane marked 'N2b mut') and lost
264 upon concomitant mutation of the N1a ΦxFG G3BP binding motif (lane marked 'N1a+N2b
265 mut') (Fig. 4C). The findings indicate that SARS-CoV-2 N-G3BP interaction is not required for
266 inhibition of the ISR, at least not upon induction of the ISR via the PKR signaling pathway
267 under the conditions applied. Moreover, this interaction is also not sufficient to prevent PKR-
268 induced formation of SGs or to promote their disassembly.
269 To study whether G3BP-binding might still affect SG formation, HeLa PKR^{KO} cells were
270 transfected to express wildtype N or mutant derivatives and subjected to arsenite/heme-
271 regulated inhibitor kinase (HRI)-induced stress. This approach allowed us to study the
272 importance of N-G3BP1 interaction more directly, i.e. without transfection induced PKR
273 activation and N-mediated inhibition of PKR as complicating factors. Under these conditions,
274 N inhibited SG formation albeit to limited extent (Fig. 5). The observed reduction in the
275 number of SG-producing cells was largely abrogated upon introduction of inactivating
276 mutations in N1a and may thus be ascribed to G3BP sequestration. This phenomenon
277 seemed concentration-dependent, noticeable particularly when considering cells with high
278 expression levels of N (Fig. 5C), whereas N2b-dependent loss of PKR-induced SGs in wildtype
279 HeLa cells was already observed at very low levels of N (Fig. 1B).

280

281 **Suppression of PKR-induced ISR by coronavirus N proteins is mediated predominantly by**
282 **N2b.** To corroborate our observations, we measured N-mediated rescue of ISR-induced
283 translational arrest also by flow cytometry. To this end, we used a cotransfection assay with
284 red fluorescence protein (RFP) expressed from vector pcDNA-RFP serving as reporter (27).
285 Co-transfection with ISR-inducing plasmid pEGFP-N3 strongly inhibited RFP production (**Fig.**
286 **6**, top; see also **Fig. S4**). RFP expression was rescued in cells co-expressing N2b but not by its
287 RNA-binding deficient derivative N2b-$K^{257}A/K^{261}A$. RFP expression was also rescued by the
288 intact N proteins of either SARS-CoV-2 or HCoV-229E and to similar levels by SARS-CoV-2 N
289 mutants defective for G3BP1/2 binding (N-$R^{14}A/I^{15}A$) or N1b methylation (N-$R^{95}K$) (**Fig. 6**). In
290 contrast, inactivation of N2b through the $K^{257}A/K^{261}A$ double mutation in the intact N protein
291 of either SARS-CoV-2 or HCoV-229E significantly reduced RFP expression (**Fig. 6**). Intriguingly,
292 however, RFP expression levels were still higher than those observed for EGFP (p-value
293 0.0014) or N2b-$K^{257}A/K^{261}A$ (p-value 0.0195). The data suggest that suppression of the PKR-
294 induced ISR by coronavirus N proteins is mediated predominantly by the N2b domain though
295 not exclusively. Apparently, N counteracts translational arrest also through other domains
296 via alternative mechanisms, but this contribution only becomes detectable upon N2b
297 inactivation. Saliently, however, disruption of N-G3BP interactions through substitutions in
298 segment N1a did not have an additive effect when tested in combination with the N2b
299 mutations (**Fig. 6**; panel 'SARS2 N N1a+N2b mut').

300

301 **N2b-mediated suppression of the ISR and type I interferon response in virus-infected cells.**
302 Whereas the results provide conclusive evidence for ISR suppression upon transient
303 expression of N in transfected cells, the question arises whether this phenomenon also
304 occurs during natural infection and whether it is relevant for evasion of the innate host
305 immune response. Unfortunately, the essential functions of N at multiple stages of the
306 coronavirus life cycle, both during early replication as well was in genome packaging during
307 virion assembly, precludes a straightforward reverse genetics approach. Thus, the
308 construction of recombinant SARS-CoV-2 mutants with an N protein defective in N2b RNA
309 binding was deemed a nonviable option. We therefore resorted to a well-established
310 alternative model based on recombinant encephalomyocarditis virus mutant EMCV-L^{zn}, in

311 which the autologous ISR antagonist (the leader protein L) is inactivated. The mutant virus is
312 no longer able to counteract the ISR (63-65) and hence provides a convenient platform to
313 identify and characterize ISR antagonists of other viruses.
314 Our initial experiments were performed with an EMCV mutant that coded for a chimeric
315 polyprotein with N2b at its N-terminus, downstream of the first five residues of EMCV L^{zn}
316 that are important for efficient IRES-mediated translation (66) and two additional residues
317 encoded by an engineered *Xho*I site. This virus, however, failed to suppress the ISR. We
318 noted that in the fusion protein, two negatively charged residues, E^6 (from L) and E^8
319 (encoded by the *Xho*I sequence) are immediately upstream of N-terminal N2b residues K^{248}
320 and K^{249} (residues 9 and 10 of the chimera) and proximal to critical N2b residues K^{257} and K^{261}
321 **Fig. S5**). Arguing that this might affect N2b RNA binding, we introduced into the EMCV-L^{zn}
322 genome an N-terminally extended N2b with the N2a region serving as a spacer (**Fig. 7A**, **Fig.**
323 **S5**). Indeed, in cells, infected with the resulting virus EMCV-L^{zn}-N2aN2b^{wt}, SG formation was
324 suppressed to 30% of that caused by EMCV-Lzn, i.e. to levels similar to those reported for
325 EMCV derivatives with L replaced by established PKR inhibitor MERS-CoV ns4a (**Fig. 7B**, **C**). In
326 accordance, in cells infected with the N2aN2b^{wt} virus, levels of phosphorylated PKR were
327 consistently low, comparable to those in wildtype EMCV-infected cells and, as calculated
328 from band densities, 4.5 to 6-fold lower than those in cells infected with EMCV-L^{zn-}. Thus, in
329 its activity N2aN2b^{wt} mimicked MERS-CoV ns4a which prevents PKR activation by
330 sequestering dsRNA (27) but differed from AcP10 which inhibits the ISR at a level
331 downstream of PKR (31). Like MERS-CoV ns4a and AcP10, N2aN2b restored replication
332 efficacy of EMCV-L^{zn} to near wildtype levels as based on expression of the viral capsid
333 proteins (**Fig. 7D**).
334 To test whether N2aN2b, like ns4a, also suppresses the type I interferon response, levels
335 of IFN-β mRNA were determined by qRT-PCR. Indeed, in cells infected with EMCV-L^{zn}-
336 N2aN2b^{wt} IFN-β expression was reduced as compared to EMCV-L^{zn} infected cells to levels
337 observed in cells infected with EMCV wt or EMCV-L^{zn}-MERS-ns4a (**Fig. 7E**). In contrast, in
338 cells infected with EMCV-L^{zn}-N2aN2b-K^{257}A+K^{261}A, encoding an inactive N2b, there was no
339 detectable suppression of SG formation, PKR was phosphorylated, and viral replication was
340 delayed to similar if not larger extent than in EMCV-L^{zn}-infected cells (**Fig. 7B**, **D**). EMCV-L^{zn}-
341 N2aN2b-K^{257}A+K^{261}A also lost the capacity to suppress the type I IFN response although this

342 was noticeable only at 8 hr post infection (Fig. 7E), which may be attributed to the
343 considerable delay in virus replication and a consequential late onset of IFN induction.
344 We conclude that SARS-CoV-2 N2b functions as an antagonist of the ISR in EMCV-infected
345 cells and can functionally replace the EMCV L protein by acting as a classical PKR antagonist
346 and preventing activation of the ISR by sequestering dsRNA. This mode of action differs from
347 that of beluga whale CoV AcP10 and Aichivirus L, which counteract the ISR by salvaging
348 global translation through competitive inhibition of p-eIF2–eIF2B association (31). The data
349 lend support to the notion that N through N2b may inhibit the ISR and SG formation also in
350 the context of SARS-CoV-2-infected cells.

351 **DISCUSSION**

352 To successfully establish infection, viruses must subdue the intracellular host defense
353 long enough to complete their replication cycle and vigorously enough to prevent the
354 infected cells from raising the alarm. The detection of dsRNA, an inevitable byproduct of
355 both RNA and DNA virus replication is central to activation of the innate antiviral defense.
356 The activation of RLRs must be averted that would otherwise culminate, through intra- and
357 intercellular signaling, in the production of type I interferons and other proinflammatory
358 cytokines. Also, while host cell protein synthesis should best be inhibited and kept at a
359 minimum, efficient unperturbed production of viral proteins must be ensured by preventing
360 translational suppression due to activation of the OAS/RNaseL pathway and PKR-dependent
361 induction of the ISR. Recent publications implicated SARS-CoV-2 N protein as an inhibitor of
362 SG formation and an RLR antagonist (33-36, 67, 68). Here, we confirmed and extended these
363 observations using a convenient procedure to assess PKR-induced ISR activation based on
364 transfection of ISR-inducing plasmid DNA to drive the expression of putative ISR antagonists
365 genetically fused to EGFP. We conclusively demonstrate that SARS-CoV-2 N is endowed with
366 the ability to inhibit PKR activation, translational arrest and ensuing SG formation. Moreover,
367 we showed that the N protein of human alphacoronavirus 229E (subgenus *Duvinacovirus*)
368 can also prevent translational arrest and suppresses SG formation to a similar extent and via
369 a similar mode of action. These findings suggest that this property may be widely conserved
370 among members of different orthocoronavirus (sub)genera.

371 To study the mechanism of ISR inhibition, we performed a systematic deletion and site-
372 directed mutational analysis of SARS-CoV-N. We found that inhibition of SG formation was
373 lost upon deletion of N2b in accordance with findings of Zheng et *al.*, (35). However, we
374 crucially extend their observations by showing that N2b when expressed in isolation, is
375 sufficient to impair transfection-induced ISR-mediated translational shut off as well as the
376 formation of SGs. Apparently, N2b counteracts the ISR by binding dsRNA. Ala substitution of
377 conserved Lys residues (Lys^{257} and/or Lys^{261}) in the putative RNA-binding cleft of N2b that
378 abolished dsRNA binding also abolished ISR inhibition. Importantly, these substitutions also
379 caused the intact N proteins of SARS-CoV-2 and HCoV-229E to lose their activity as ISR
380 antagonists. The observations thus strongly support a model in which coronavirus N proteins
381 through their N2b domain prevent activation of the ISR by PKR by sequestering dsRNA, like

382 the other viral PKR inhibitors IAV ns1 and MERS-CoV ns4a that were used as controls
383 throughout.
384 The N protein plays a crucial role during the very early steps of the CoV infection cycle
385 (55, 69-71) and is indispensable for virus morphogenesis. Evidently, this impedes a direct
386 mutational reverse genetics approach to study the occurrence and relevance of N-mediated
387 inhibition of the ISR in CoV-infected cells. However, by using a mutant EMCV as a platform,
388 we showed that an extended protein N2aN2b can functionally replace the autologous
389 enterovirus L protein and can salvage the EMCV replication defect caused by L inactivation,
390 like we previously showed for MERS-CoV ns4a and BWCoV AcP10 (27, 31). Like MERS-CoV
391 ns4a, but unlike BWCoV AcP10 -which blocks the ISR downstream of PKR-, N2aN2b
392 prevented PKR phosphorylation apparently via N2b-mediated RNA binding. The findings
393 provide proof of principle that N2b can promote viral replication by preventing PKR and
394 ensuing ISR activation, supporting the notion that N through its N2b domain may do so as
395 well during CoV infection.
396 Adding relevance to our observations, selection for enhanced innate immune escape
397 apparently favored SARS-CoV-2 variants with increased N expression (72). Moreover, a
398 three-nucleotide change in Gamma also present in Alpha and Omicron variants of concern
399 created a new (cryptic) transcription regulating sequence to drive the synthesis of a novel
400 subgenomic mRNA species from which a truncated N-protein, N*, may be translated
401 corresponding with the C-terminus of the protein and initiating at in frame Met^{210} (72, 73). If
402 N* is indeed expressed, our findings strongly support a role in dsRNA sequestration and
403 innate antagonism.
404 The native coronavirus N proteins are subject to extensive posttranslational modifications
405 in domains and segments other than N2b. Some have been implicated in liquid-liquid phase
406 separation (62, 74), RNA binding (33), SG formation and inhibition of innate immunity (33,
407 62), prompting the question whether these modifications promote or hinder its function as
408 an ISR antagonist. Reportedly, methylation of Arg^{95} in the SARS-CoV-2 N1b segment by host
409 protein arginine methyltransferases is required for RNA binding and for the inhibition of
410 arsenite-induced formation of G3BP1-containing SGs (33). In our hands, however, an N
411 mutant with Arg^{95}Lys substitution, described to block N-mediated suppression of SGs (33),
412 still prevented PKR-induced ISR-associated translational repression to identical extent as the
413 wildtype protein and likewise prevented SG formation. In another recent study, Wang et *al.*

414 (62) reported suppression of MAVS signaling by intact SARS-CoV-2 N protein but not by an N
415 derivative from which N2b had been deleted. They attributed this to N-induced and N2b-
416 dependent liquid-liquid phase separation (LLPS) subject to acetylation of N3 residue Lys^{375}.
417 In accordance, we find that in EMCV-infected cells, N2aN2b, like MERS4a, suppresses β-
418 interferon (IFN-β) expression and show that this activity is blocked by mutations that abolish
419 N2b-mediated RNA binding. In apparent contrast to the observations of Wang et *al*. (62),
420 however, we find that acetylation of Lys^{375} is not essential for RNA binding by N2b and that
421 Lys^{375}Arg substitution does not detectably affect inhibition of the PKR-induced ISR by the
422 intact N protein. Our findings suggest that N, through the autonomous activity of the N2b
423 domain, acts not only as a classical PKR inhibitor to thwart ISR activation but may also
424 prevent RLR activation and thus block induction of the type I IFN response, whether directly
425 by shielding dsRNA or indirectly by preventing SGs to act as platform for immune signaling.
426 The interaction between N and SG scaffold proteins G3BP1 and -2 mediated through the
427 N1a ΦxFG motif (33, 37-40), was recently concluded to be the main determinant in SG
428 disassembly (38). Our current findings would seem to be at odds with this view, but in
429 accordance with observations by these authors, we did observe that functional disruption of
430 the critical ΦxFG motif abrogated inhibition of SG formation in arsenite-treated HeLa PKR^{KO}
431 cells. Our findings, however, would suggest that sequestration of the G3BPs to prevent
432 assembly of SG or to promote their disassembly requires high expression levels of N.
433 Importantly, N proteins with intact N1a domain but with mutations in N2b that abolish RNA
434 binding failed to prevent SG formation in HeLa wt cells. Also, the 229E N protein lacks a
435 ΦxFG motif, yet inhibits formation of SGs via the same N2b-dependent mechanism as SARS-
436 CoV-2 N. The findings may be reconciled, however, by assuming that sarbecovirus N proteins
437 have been evolutionary selected to interfere with G3BP function, possibly even beyond the
438 formation and function of SGs (75), through distinct mechanisms at multiple levels during
439 different stages of the viral life cycle, mediated by different domains and regulated by
440 distinct posttranslational modifications, and perhaps subject to protein distribution and
441 availability of viral genomes for encapsidation. Such subtleties may be missed in over-
442 expression experiments and overshadowed by the robust inhibition of the PKR-triggered ISR
443 by N2b. Hence, in coronavirus-infected cells, N1a-mediated G3BP-N association (38, 40, 54)
444 and N2b-mediated dsRNA binding (36) may well act in concert to hamper SG assembly and
445 to impede recruitment and SG-facilitated activation of RLRs and PKR (20-23). Indeed, this

446 would be consistent with observations by others (35, 36) of SARS-CoV-2 N suppressing SG-
447 associated RLR activation and inhibiting induction of type I IFNs by targeting G3BP1. The
448 relative importance of dsRNA shielding, G3BP recruitment and other activities of N for
449 suppression of innate immunity during coronavirus infection clearly deserves further study.
450

451 **MATERIALS AND METHODS**

452

453 **Cell lines.** HeLa-R19, HeLa R19 PKR^{KO} (27), A549 and BHK21 cells were maintained in
454 Dulbecco's Modified Eagle's Medium (DMEM) supplemented with 10% (V/V) fetal calf serum
455 (FCS) and 100 units/ml penicillin and streptomycin. All cell lines were routinely tested
456 negative for mycoplasma contamination.

457 **Recombinant EMCV viruses.** Recombinant EMCV viruses were derived from the pM16.1-
458 derived pStrep2-VFETQG-Zn-M16.1 infectious clone (27, 76). This vector carries a Zn-finger
459 mutation to inactivate EMCV L as well as coding sequences for a Strep2-tag and a synthetic
460 optimized 3C^{pro} recognition site (VFETQG). The coding sequences for N2b and N2a2b were
461 PCR amplified from SARS-CoV-2-derived cDNA (sequences deposited in EVA database; Ref-
462 SKU: 026V-03883) and inserted into XhoI/NotI-digested pStrep2-VFETQG-Zn-M16.1 yielding
463 pStrep2-SARS-CoV-2-N2b-VFETQG-Zn-M16.1 and pStrep2-SARS-CoV-2-N2aN2b-VFETQG-Zn-
464 M16.1, respectively. Mutations to substitute N2b Lys^{257} and Lys^{261} by Ala were introduced by
465 Q5 side-directed mutagenesis (New England Biolabs, NEB) generating pStrep2-SARS-CoV-2-
466 N2aN2b K^{257}A/K^{261}A-VFETQG-Zn-M16.1. The vectors were linearized with BamHI, used for *in*
467 *vitro* transcription with the RiboMAX kit (Promega) and the resulting RNA was purified using
468 the NucleoSpin RNA mini kit (Machery-Nagel) following the manufacturer's protocol. Viruses
469 were recovered by transfecting BHK-21 cells, grown to subconfluency in T125 flasks, with 1.5
470 µg of the run-off RNA transcripts using Lipofectamine2000 (Invitrogen) transfection reagent
471 according to the manufacturer's protocol. After 2-4 days, when total cytopathic effect was
472 apparent, the cultures were subjected to three freeze-thaw cycles, cell debris was pelleted
473 at 4,000x*g* for 15 minutes and virus was concentrated from the supernatants by
474 ultracentrifugation though a 30% sucrose cushion at 140,000x*g* for 16 hrs at 4°C in a SW32Ti
475 rotor. Virus pellets were resuspended in phosphate-buffer saline (PBS). The viruses were
476 characterized by isolating viral RNA from 150-µL aliquots of the cell culture supernatant with
477 the NucleoSpin RNA Virus kit (Macherey-Nagel) followed by conventional RT-PCR and
478 bidirectional Sanger sequence analysis of the inserted SARS-CoV-2 sequences and flanking
479 regions. Viral titers, determined by endpoint titration and calculated by the Spearman-
480 Kaerber formula, are averages from three independent experiments.

481 **Plasmids for eukaryotic and prokaryotic expression.** Eukaryotic expression plasmids were
482 constructed by cloning PCR-amplified sequences of interests, flanked by NheI and BamHI
483 restriction sites, into NheI/BamHI digested vector pEGFP-N3 (ClonTech) such that the
484 encoded viral proteins are C-terminally fused to enhanced green fluorescent protein (EGFP).
485 pcDNA-RFP was purchased from Addgene.
486 Procaryotic expression plasmid pGEX2T-Hisx6-N2b encoding N-terminally His-tagged
487 SARS-CoV-2 N2b was created by linearizing vector pGEX2T, amplifying the N2b coding
488 sequences by Q5-PCR, and assembling the fragments by NEBuilder HiFi DNA Assembly (NEB)
489 according to the manufacturer's instructions. Mutations (N2b $K^{257}A$, N2b $K^{261}A$ and N2b
490 $K^{257}A+K^{261}A$) were generated by Q5 site-directed mutagenesis (New England Biolabs, NEB).
491 All constructs were sequenced to confirm their integrity. There were no major differences in
492 transfection efficiency (**Fig. S6**)
493
494 **Immunofluorescence assay.** HeLa-R19 wt, HeLa-R19 PKR^{KO} cells and A549 cells were seeded
495 onto 12 mm glass cover slips in 24-well plates (Corning Costar) at $5x10^4$ cells and grown for
496 24 hr. They were then transfected with 500 ng total DNA/well using Lipofectamine2000
497 (Invitrogen) according to the instructions of the manufacturer. At 24 hr post transfection,
498 cells were either left untreated or treated with 500 µM sodium arsenite ($NaAsO_2$, Riedel-de
499 Haën) for 30 min at 37°C and subsequently fixed in PBS + 3.7% paraformaldehyde (PFA).
500 Vero E6-TMPRSS2 cells were infected with SARS-CoV-2 Wuhan (D614G) or Omicron BA.1
501 variants at a multiplicity of infection (MOI) of 5 $TCID_{50}$/cell and HeLa-R19 cells were infected
502 with recombinant EMCV viruses at an MOI of 10 $TCID_{50}$/cell and incubated for times
503 indicated in the text. Cells were fixed with paraformaldehyde (3.7% in PBS), incubated with
504 PBS + 0.1% glycine for 10 min to quench the fixative, permeabilized with 0.1% Triton X-
505 100/PBS+s for 10 min at RT and subsequently blocked in blocking buffer (PBS + 1% BSA +
506 0.1% Tween-20) for 30min in a dark humidified chamber at 37°C. The cells were then
507 incubated in blocking buffer containing mouse anti-dsRNA (1:1000; English & Scientific
508 Consulting), goat anti-eIF3η (1:200, SantaCruz) and rabbit anti-G3BP2 (1:200; Bethyl
509 Laboratories) for 1h at room temperature (RT). After three washing steps with
510 PBS+0.1%Tween-20, cells were incubated with secondary antibody donkey anti-mouse Cy2
511 (1:100; The Jackson Laboratory), donkey anti-goat Alexa594 (1:200; Invitrogen), donkey anti-
512 rabbit Alexa647 (1:200; Invitrogen) in block buffer for 1h at RT. The cells were then washed

513 three times with PBS+0.1%Tween-20, once with distilled water and mounted on glass
514 microscope slides in ProLong Diamond Antifade (Invitrogen) mounting medium. Cells were
515 examined by conventional wide-field (Olympus) and confocal immunofluorescence
516 microscopy (Nikon A1R) in most cases also in a blinded fashion by a second independent
517 observer.
518
519 **Flowcytometry analysis.** HeLa cells were seeded in a 12-well cluster (10^5 cells/well) and,
520 after overnight incubation, transfected with the indicated plasmids (500 ng well; 250
521 ng/plasmid) using Lipofecatmine2000 (Invitrogen) according to the manufacturer's
522 instructions. At 24 hr post transfection, cells were detached with trypsin, washed once PBS,
523 and fixed in PBS, 3.7% PFA for 10 min. The samples were washed once in FACS buffer (PBS +
524 0.02% Na-azide and 0.5% BSA) and kept in FACS buffer at 4ºC. RFP fluorescence intensity was
525 recorded with a CytoFLEX LX flow cytometer (Beckman Coulter) and the data were analyzed
526 by FlowJo™ v10 software (BD Biosciences). Samples were gated for live single cell
527 populations and then gated for negative, low (L) and high (H) RFP expressing cells. For bar
528 graphs [H/L] ratios were normalized with the ratio calculated for the relevant wildtype
529 protein set at 100%.
530
531 **Electrophoretic Mobility Shift Assay (EMSA).** To purify the wildtype N2b domain and its
532 mutated derivatives, *E. coli* BL21 cells (Sigma-Aldrich), transformed with pGEX2T-Hisx6-N2b
533 or its mutated derivatives, were grown in LB medium containing ampicillin (50 µg/ml) at
534 37°C until the optical density at 600 nm (OD_{600nm}) reached 0.3. The temperature was then
535 reduced to 18°C, and when the OD_{600nm} reached 0.5, protein expression was induced with
536 0.5 mM IPTG. Following expression for 16 hrs, the cells were harvested by centrifugation and
537 resuspended in lysis buffer (100 mM Tris-HCl pH=8, 300 mM NaCl, 10 mM imidazole, 0.1%
538 Triton X-100, 5% Glycerol) complemented with lysozyme (0.25 mg/ml; Merk) and cOmplete
539 Protease Inhibitor (Roche). The samples were sonicated and centrifuged at 15,000*g* for 45
540 min at 4°C to pellet cell debris. The cleared lysates were passed through a 0.45-µm filter and
541 incubated with 1 ml of Ni-NTA (nitrilotriacetic acid) resin (Thermo Scientific) at 4°C over-
542 night (O/N) on a roller. The beads were washed twice with wash buffer (100mM Tris-HCl (pH
543 8.0), 300mM NaCl, 10mM Imidazole) and then eluted with a buffer consisting of 100 mM

544 Tris-HCl, 300 mM NaCl, and 500 mM imidazole (pH 8). The eluted proteins were subjected
545 to dialysis in 20mM Tris-HCl, 150mM NaCl and flash-frozen in 20-µl aliquots.
546 For the EMSA, 1 µM of a 32-mer single stranded RNA oligonucleotides corresponding to
547 SARS-CoV-2 (GenBank accession no. MZ558051.1) sequence 5'-
548 CGAGGCCACGCGGAGUACGAUCGAGGGUACAG-3' and a scrambled version thereof, 5'-
549 GGCACGGAGUAUACCGGACGAGCGGAACGGCU-3', each were mixed 1 :1 with their
550 respective complimentary RNA oligonucleotides in denaturing buffer (10 mM $NaH_2PO_4 \cdot H_2O$,
551 50 mM NaCl, 1 mM EDTA, 0.01% NaN_3, pH 7.4 at 25°C), incubated at 90°C for 4 min and then
552 allowed to anneal at RT for 30 min. For the ssRNA sample preparation, the oligonucleotide
553 was diluted in denaturing buffer, incubated at 90°C for 30 sec to destroy possible secondary
554 structures and rapidly cooled on ice. Proteins were diluted in protein buffer (20mM Tris-HCl
555 (pH=8), 150mM NaCl) to a concentration of 100 ng/µl and mixed in 10X, 20X or 40X fold
556 molar excess with 10 ng ssRNA or 10 ng dsRNA in binding buffer (20 mM Tris-HCl, 100 mM
557 NaCl, 1 mM EDTA, 1mM TCEP, 0.02% Tween-20, pH 7.0 at 25°C) in 5 µl reaction volumes. The
558 samples were incubated for 30 min on ice, then supplemented with glycerol to a final
559 concentration of 5% (v/v) and separated in ultrathin (10 ml; 75 x 50 mm) RNase-free 1%
560 agarose gels in 0.5x TB buffer (45 mM Tris base, 45 mM boric acid, pH 8.2-8.5) at 200V. RNAs
561 were stained by incubating the gels in 50 ml 2X Invitrogen™ SYBR™ Gold nucleic acid gel
562 stain (ThermoFisher) in 0.5x TB buffer, diluted from a 10.000X concentrate, for 15 min under
563 agitation and de-stained for 21 min with 0.5 X TB buffer refreshing the buffer 3 times.
564 Stained RNA was visualized with the Gel Doc System (BioRad).
565
566 **Western-blot analysis.** HeLa R19 wt and PKR^{KO} cells were seeded in 6-well clusters ($4x10^5$
567 cells/well) and after a 16 hr recovery were infected with recombinant EMCVs at MOI 10 or
568 tranfected with plasmids as indicated in the text. The infection was allowed to proceed for 6
569 or 8 hrs and transfections for 24 hrs. Cells were then released by trypsin and lysed in ice-cold
570 lysis buffer (Tris-HCl pH 8.0, 50mM, NaCl 150mM, EDTA 1mM, NP40 1%, cOmplete Mini
571 Protease Inhibitor Cocktail (Roche) and phosphatase inhibitor PhosSTOP (Roche)) for 30 min
572 at 4°C under constant agitation. Cell debris was pelleted for 20 min 12000 rpm at 4°C.
573 Cleared lysates were harvested and protein concentrations determined by the Pierce BCA
574 assay (ThermoFisher Scientific) according to the manufacturer's instructions. Samples of
575 each lysate, corresponding to 100 µg protein, were separated by SDS-PAGE in reducing 10%

576 polyacrylamide gels. The proteins were then blotted onto 0.2 µm nitrocellulose membranes
577 by wet electrophoretic transfer or semi-dry transfer. Membranes were washed three times
578 in TBST (20 mM Tris, 150 mM NaCl + 0.1% Tween-20), 5 min each, and incubated in blocking
579 buffer (TBST + 2% BSA) for 1h at RT. Membranes were successively incubated with primary
580 antibodies diluted in blocking buffer (mouse anti-G3BP1, 1:4000, BD Biosciences, rabbit anti-
581 GFP, 1:1000, ThermoFisher, mouse anti-PKR, 1:1000, BD Biosciences; rabbit anti-PKR-P,
582 1:1000, Abcam; mouse anti-βactin, 1:5000, Invitrogen; rabbit anti-mengovirus capsid,
583 1:1000, kindly provided by Prof. Ann Palmenberg) for 16 hr at 4°C, and then for 30 min at RT
584 with goat-α-mouse-IRDye680 (Li-COR, 1:15000) or goat-α-rabbit-IRDye800 (Li-COR, 1:15000)
585 diluted in blocking buffer. Between and after the incubations, the membranes were washed,
586 thrice each time, with TBST. Finally, membranes were washed once with PBS and scanned
587 using an Odyssey Imager (Li-COR). ImageJ was used to quantitate and compare density of
588 bands after correction with beta-actin as loading control.
589
590 **Co-immunoprecipitation (Co-IP) assay.** HeLa R19 wt and PKR^{KO} cells were seeded in 6-well
591 clusters (4x10^{5} cells/well) and, after a 16 hr recovery, transfected with the indicated
592 plasmids. At 24 hrs post transfection, cells were washed once in PBS, released by trypsin and
593 incubated in ice-cold lysis buffer (Tris-HCl pH 8.0, 50mM, NaCl 150mM, EDTA 1mM, NP40
594 1%, cOmplete Mini Protease Inhibitor Cocktail (Roche) and phosphatase inhibitor PhosSTOP
595 (Roche)) for 30 min on ice. The cell lysates were cleared in a microcentrifuge for 10 min at
596 12000 rpm at 4°C. Supernatants were harvested and incubated with 25 µl of preequilibrated
597 GFP-Trap agarose beads (ChromoTek) for 1h at 4°C with end-over-end rotation. Beads were
598 then washed 3 times with wash buffer (Tris-HCl pH 8.0, 50mM, NaCl 150mM, EDTA 1mM).
599 Bound proteins were eluted in 80 µl 2x SDS-sample buffer, separated by SDS-PAGE in
600 reducing 8% polyacrylamide gels and analyzed by Western blotting.
601
602 **RT-qPCR analysis.** HeLa R19 cells, seeded in 24-well clusters (5x10^{4} cells/well), were
603 inoculated with recombinant EMCVs at MOI 10 as above. At 6 or 8 hrs post infection cells
604 were lysed and cellular RNA was isolated using the total RNA isolation kit (Machery-Nagel)
605 according to manufacturer's instructions. Reverse transcription was set up using TaqMan
606 Reverse Transcription Reagents (Applied Biosystem) as indicated in the manufacturer's
607 instructions. qPCR analysis of human IFN-β, human actin mRNA and EMCV viral RNA was

608 performed mixing the Fast SYBR green Master Mix (ThermoFisher) with cDNA and 1µM of
609 the forward and reverse corresponding primers: IFN-β (5'-ATGACCAACAAGTGTCTCCTCC-3'
610 and 5'-GCTCATGGAAAGAGCTGTAGTG-3'), actin (5'-CCTTCCTGGGCATGGAGTCCTG-3' and
611 5'GGAGCAATGATCTTGATCTTC-3') and EMCV RNA (5'-TCTGTTCTGCCTGTGTTTG-3' and 5'-
612 AAAGAAGAGGGTGCCGAAAT-3'). Amplification occurred in a Roche Light Cycler using the
613 following program: polymerase activation (95°C for 5min), amplification (45 cycles: 95°C for
614 10 sec, 60°C for 5 sec, 72°C for 30 sec), melting curve (95°C for 5 sec, 65°C for 1 min) and
615 cooling (40°C for 10 sec). The experiments were carried out in triplex for each data point.
616 The relative quantification of the IFN-β gene expression was determined using the $2^{-\Delta\Delta Ct}$
617 method (77), then the relative IFN-β mRNA levels were normalized to the EMCV-zn IFN-β
618 mRNA level set as 100.
619
620

ACKNOWLEDGMENTS AND FUNDING SOURCES

We would like to thank Huib H. Rabouw for helpful comments and discussions, Richard Wubbolts and Ester van t Veld from the Center for Cell Imaging for the microscopy support and Ger Arkesteijn and Estefania Lozano Andres from the Flow Cytometry and Cell Sorting Facility for the flow cytometry support.

This work was supported by the European Union (Horizon 2020 Marie Skłodowska-Curie ETN "INITIATE", grant agreement number 813343) and by the Dutch Research Council NWO OCENW.KLEIN.344.

630 **REFERENCES**

631

632 1. S. Hur, Double-Stranded RNA Sensors and Modulators in Innate Immunity. *Annual Review of*
633 *Immunology* **37**, 349-375 (2019).
634 2. D. H. Wreschner, J. W. McCauley, J. J. Skehel, I. M. Kerr, Interferon action—sequence
635 specificity of the ppp(A2'p)nA-dependent ribonuclease. *Nature* **289**, 414-417 (1981).
636 3. J. B. Andersen, K. Mazan-Mamczarz, M. Zhan, M. Gorospe, B. A. Hassel, Ribosomal protein
637 mRNAs are primary targets of regulation in RNase-L-induced senescence. *RNA Biol* **6**, 305-315
638 (2009).
639 4. Y. Li *et al.*, Activation of RNase L is dependent on OAS3 expression during infection with
640 diverse human viruses. *Proceedings of the National Academy of Sciences* **113**, 2241-2246
641 (2016).
642 5. J. Donovan, S. Rath, D. Kolet-Mandrikov, A. Korennykh, Rapid RNase L-driven arrest of
643 protein synthesis in the dsRNA response without degradation of translation machinery. *Rna*
644 **23**, 1660-1671 (2017).
645 6. J. M. Burke, S. L. Moon, T. Matheny, R. Parker, RNase L Reprograms Translation by
646 Widespread mRNA Turnover Escaped by Antiviral mRNAs. *Mol Cell* **75**, 1203-1217.e1205
647 (2019).
648 7. S. L. Schwartz, G. L. Conn, RNA regulation of the antiviral protein 2'-5'-oligoadenylate
649 synthetase. *Wiley Interdiscip Rev RNA* **10**, e1534 (2019).
650 8. A. G. Hinnebusch, The scanning mechanism of eukaryotic translation initiation. *Annu Rev*
651 *Biochem* **83**, 779-812 (2014).
652 9. J. L. Llácer *et al.*, Conformational Differences between Open and Closed States of the
653 Eukaryotic Translation Initiation Complex. *Mol Cell* **59**, 399-412 (2015).
654 10. M. Yoneyama, M. Jogi, K. Onomoto, Regulation of antiviral innate immune signaling by
655 stress-induced RNA granules. *The Journal of Biochemistry* **159**, 279-286 (2016).
656 11. Y. Wu, Z. Zhang, Y. Li, Y. Li, The Regulation of Integrated Stress Response Signaling Pathway
657 on Viral Infection and Viral Antagonism. *Frontiers in Microbiology* **12** (2022).
658 12. N. Kedersha *et al.*, Evidence that ternary complex (eIF2-GTP-tRNA(i)(Met))-deficient
659 preinitiation complexes are core constituents of mammalian stress granules. *Mol Biol Cell* **13**,
660 195-210 (2002).
661 13. M. D. Panas, P. Ivanov, P. Anderson, Mechanistic insights into mammalian stress granule
662 dynamics. *J Cell Biol* **215**, 313-323 (2016).
663 14. S. Hofmann, N. Kedersha, P. Anderson, P. Ivanov, Molecular mechanisms of stress granule
664 assembly and disassembly. *Biochim Biophys Acta Mol Cell Res* **1868**, 118876 (2021).
665 15. H. Tourrière *et al.*, The RasGAP-associated endoribonuclease G3BP assembles stress
666 granules. *J Cell Biol* **160**, 823-831 (2003).
667 16. N. Gilks *et al.*, Stress granule assembly is mediated by prion-like aggregation of TIA-1. *Mol*
668 *Biol Cell* **15**, 5383-5398 (2004).
669 17. J. R. Wheeler, T. Matheny, S. Jain, R. Abrisch, R. Parker, Distinct stages in stress granule
670 assembly and disassembly. *eLife* **5**, e18413 (2016).
671 18. J. Guillén-Boixet *et al.*, RNA-Induced Conformational Switching and Clustering of G3BP Drive
672 Stress Granule Assembly by Condensation. *Cell* **181**, 346-361.e317 (2020).
673 19. P. Yang *et al.*, G3BP1 Is a Tunable Switch that Triggers Phase Separation to Assemble Stress
674 Granules. *Cell* **181**, 325-345.e328 (2020).
675 20. K. Onomoto *et al.*, Critical role of an antiviral stress granule containing RIG-I and PKR in viral
676 detection and innate immunity. *PLoS One* **7**, e43031 (2012).
677 21. J. S. Yoo *et al.*, DHX36 enhances RIG-I signaling by facilitating PKR-mediated antiviral stress
678 granule formation. *PLoS Pathog* **10**, e1004012 (2014).

679 22. L. C. Reineke, R. E. Lloyd, The stress granule protein G3BP1 recruits protein kinase R to
680 promote multiple innate immune antiviral responses. *J Virol* **89**, 2575-2589 (2015).
681 23. W. Yang *et al.*, G3BP1 inhibits RNA virus replication by positively regulating RIG-I-mediated
682 cellular antiviral response. *Cell Death & Disease* **10**, 946 (2019).
683 24. X. Deng *et al.*, Coronavirus nonstructural protein 15 mediates evasion of dsRNA sensors and
684 limits apoptosis in macrophages. *Proc Natl Acad Sci U S A* **114**, E4251-e4260 (2017).
685 25. E. Kindler *et al.*, Early endonuclease-mediated evasion of RNA sensing ensures efficient
686 coronavirus replication. *PLoS Pathog* **13**, e1006195 (2017).
687 26. J. Zhao *et al.*, Coronavirus Endoribonuclease Ensures Efficient Viral Replication and Prevents
688 Protein Kinase R Activation. *J Virol* **95** (2020).
689 27. H. H. Rabouw *et al.*, Middle East Respiratory Coronavirus Accessory Protein 4a Inhibits PKR-
690 Mediated Antiviral Stress Responses. *PLoS Pathog* **12**, e1005982 (2016).
691 28. K. Nakagawa, K. Narayanan, M. Wada, S. Makino, Inhibition of Stress Granule Formation by
692 Middle East Respiratory Syndrome Coronavirus 4a Accessory Protein Facilitates Viral
693 Translation, Leading to Efficient Virus Replication. *J Virol* **92** (2018).
694 29. J. M. Thornbrough *et al.*, Middle East Respiratory Syndrome Coronavirus NS4b Protein
695 Inhibits Host RNase L Activation. *mBio* **7**, e00258 (2016).
696 30. S. A. Goldstein *et al.*, Lineage A Betacoronavirus NS2 Proteins and the Homologous Torovirus
697 Berne pp1a Carboxy-Terminal Domain Are Phosphodiesterases That Antagonize Activation of
698 RNase L. *J Virol* **91** (2017).
699 31. H. H. Rabouw *et al.*, Inhibition of the integrated stress response by viral proteins that block p-
700 eIF2–eIF2B association. *Nature Microbiology* **5**, 1361-1373 (2020).
701 32. B. Gao *et al.*, Inhibition of anti-viral stress granule formation by coronavirus
702 endoribonuclease nsp15 ensures efficient virus replication. *PLoS Pathog* **17**, e1008690
703 (2021).
704 33. T. Cai, Z. Yu, Z. Wang, C. Liang, S. Richard, Arginine methylation of SARS-Cov-2 nucleocapsid
705 protein regulates RNA binding, its ability to suppress stress granule formation, and viral
706 replication. *J Biol Chem* **297**, 100821 (2021).
707 34. L. Luo *et al.*, SARS-CoV-2 nucleocapsid protein phase separates with G3BPs to disassemble
708 stress granules and facilitate viral production. *Sci Bull (Beijing)* **66**, 1194-1204 (2021).
709 35. Z.-Q. Zheng, S.-Y. Wang, Z.-S. Xu, Y.-Z. Fu, Y.-Y. Wang, SARS-CoV-2 nucleocapsid protein
710 impairs stress granule formation to promote viral replication. *Cell Discovery* **7**, 38 (2021).
711 36. H. Liu *et al.*, SARS-CoV-2 N Protein Antagonizes Stress Granule Assembly and IFN Production
712 by Interacting with G3BPs to Facilitate Viral Replication. *J Virol* **96**, e0041222 (2022).
713 37. D. E. Gordon *et al.*, A SARS-CoV-2 protein interaction map reveals targets for drug
714 repurposing. *Nature* **583**, 459-468 (2020).
715 38. T. Kruse *et al.*, Large scale discovery of coronavirus-host factor protein interaction motifs
716 reveals SARS-CoV-2 specific mechanisms and vulnerabilities. *Nature Communications* **12**,
717 6761 (2021).
718 39. J. Li *et al.*, Virus-Host Interactome and Proteomic Survey Reveal Potential Virulence Factors
719 Influencing SARS-CoV-2 Pathogenesis. *Med (N Y)* **2**, 99-112.e117 (2021).
720 40. M. Biswal, J. Lu, J. Song, SARS-CoV-2 Nucleocapsid Protein Targets a Conserved Surface
721 Groove of the NTF2-like Domain of G3BP1. *J Mol Biol* **434**, 167516 (2022).
722 41. K. H. Mellits, T. Pe'ery, L. Manche, H. D. Robertson, M. B. Mathews, Removal of double-
723 stranded contaminants from RNA transcripts: synthesis of adenovirus VA RNA 1 from a T7
724 vector. *Nucleic Acids Research* **18**, 5401-5406 (1990).
725 42. F. Terenzi *et al.*, The antiviral enzymes PKR and RNase L suppress gene expression from viral
726 and non-viral based vectors. *Nucleic Acids Research* **27**, 4369-4375 (1999).
727 43. T. Gantke *et al.*, Ebola virus VP35 induces high-level production of recombinant TPL-2-ABIN-
728 2-NF-κB1 p105 complex in co-transfected HEK-293 cells. *Biochem J* **452**, 359-365 (2013).
729 44. K. R. Hurst, C. A. Koetzner, P. S. Masters, Identification of in vivo-interacting domains of the
730 murine coronavirus nucleocapsid protein. *J Virol* **83**, 7221-7234 (2009).

731 45. K. R. Hurst, R. Ye, S. J. Goebel, P. Jayaraman, P. S. Masters, An interaction between the
732 nucleocapsid protein and a component of the replicase-transcriptase complex is crucial for
733 the infectivity of coronavirus genomic RNA. *J Virol* **84**, 10276-10288 (2010).
734 46. C. K. Chang, M. H. Hou, C. F. Chang, C. D. Hsiao, T. H. Huang, The SARS coronavirus
735 nucleocapsid protein--forms and functions. *Antiviral Res* **103**, 39-50 (2014).
736 47. Q. Ye, A. M. V. West, S. Silletti, K. D. Corbett, Architecture and self-assembly of the SARS-CoV-
737 2 nucleocapsid protein. *Protein Sci* **29**, 1890-1901 (2020).
738 48. T. Y. Peng, K. R. Lee, W. Y. Tarn, Phosphorylation of the arginine/serine dipeptide-rich motif
739 of the severe acute respiratory syndrome coronavirus nucleocapsid protein modulates its
740 multimerization, translation inhibitory activity and cellular localization. *Febs j* **275**, 4152-4163
741 (2008).
742 49. E. Nikolakaki, T. Giannakouros, SR/RS Motifs as Critical Determinants of Coronavirus Life
743 Cycle. *Front Mol Biosci* **7**, 219 (2020).
744 50. C. A. Koetzner, K. R. Hurst-Hess, L. Kuo, P. S. Masters, Analysis of a crucial interaction
745 between the coronavirus nucleocapsid protein and the major membrane-bound subunit of
746 the viral replicase-transcriptase complex. *Virology* **567**, 1-14 (2022).
747 51. R. Molenkamp, W. J. Spaan, Identification of a specific interaction between the coronavirus
748 mouse hepatitis virus A59 nucleocapsid protein and packaging signal. *Virology* **239**, 78-86
749 (1997).
750 52. L. Kuo, C. A. Koetzner, K. R. Hurst, P. S. Masters, Recognition of the murine coronavirus
751 genomic RNA packaging signal depends on the second RNA-binding domain of the
752 nucleocapsid protein. *J Virol* **88**, 4451-4465 (2014).
753 53. K. R. Hurst, C. A. Koetzner, P. S. Masters, Characterization of a critical interaction between
754 the coronavirus nucleocapsid protein and nonstructural protein 3 of the viral replicase-
755 transcriptase complex. *J Virol* **87**, 9159-9172 (2013).
756 54. W. Huang *et al.*, Molecular determinants for regulation of G3BP1/2 phase separation by the
757 SARS-CoV-2 nucleocapsid protein. *Cell Discovery* **7**, 69 (2021).
758 55. C. Y. Chen *et al.*, Structure of the SARS coronavirus nucleocapsid protein RNA-binding
759 dimerization domain suggests a mechanism for helical packaging of viral RNA. *J Mol Biol* **368**,
760 1075-1086 (2007).
761 56. M. Yang *et al.*, Structural Insight Into the SARS-CoV-2 Nucleocapsid Protein C-Terminal
762 Domain Reveals a Novel Recognition Mechanism for Viral Transcriptional Regulatory
763 Sequences. *Front Chem* **8**, 624765 (2020).
764 57. M. Takeda *et al.*, Solution structure of the c-terminal dimerization domain of SARS
765 coronavirus nucleocapsid protein solved by the SAIL-NMR method. *J Mol Biol* **380**, 608-622
766 (2008).
767 58. R. Zhou, R. Zeng, A. von Brunn, J. Lei, Structural characterization of the C-terminal domain of
768 SARS-CoV-2 nucleocapsid protein. *Mol Biomed* **1**, 2 (2020).
769 59. M. P. Robertson *et al.*, The structure of a rigorously conserved RNA element within the SARS
770 virus genome. *PLoS Biol* **3**, e5 (2005).
771 60. E. Nikolakaki *et al.*, RNA association or phosphorylation of the RS domain prevents
772 aggregation of RS domain-containing proteins. *Biochim Biophys Acta* **1780**, 214-225 (2008).
773 61. C. R. Carlson *et al.*, Phosphoregulation of Phase Separation by the SARS-CoV-2 N Protein
774 Suggests a Biophysical Basis for its Dual Functions. *Mol Cell* **80**, 1092-1103.e1094 (2020).
775 62. S. Wang *et al.*, Targeting liquid–liquid phase separation of SARS-CoV-2 nucleocapsid protein
776 promotes innate antiviral immunity by elevating MAVS activity. *Nature Cell Biology* **23**, 718-
777 732 (2021).
778 63. F. Borghese, T. Michiels, The Leader Protein of Cardioviruses Inhibits Stress Granule
779 Assembly. *Journal of Virology* **85**, 9614-9622 (2011).
780 64. F. Borghese, F. Sorgeloos, T. Cesaro, T. Michiels, The Leader Protein of Theiler's Virus
781 Prevents the Activation of PKR. *J Virol* **93** (2019).

65. L. J. Visser *et al.*, Foot-and-Mouth Disease Virus Leader Protease Cleaves G3BP1 and G3BP2 and Inhibits Stress Granule Formation. *J Virol* **93** (2019).
66. A. Kaminski, G. J. Belsham, R. J. Jackson, Translation of encephalomyocarditis virus RNA: parameters influencing the selection of the internal initiation site. *Embo j* **13**, 1673-1681 (1994).
67. S. Nabeel-Shah *et al.*, SARS-CoV-2 nucleocapsid protein binds host mRNAs and attenuates stress granules to impair host stress response. *iScience* **25**, 103562 (2022).
68. Y. Zheng *et al.*, SARS-CoV-2 NSP5 and N protein counteract the RIG-I signaling pathway by suppressing the formation of stress granules. *Signal Transduction and Targeted Therapy* **7**, 22 (2022).
69. C. A. de Haan, H. Vennema, P. J. Rottier, Assembly of the coronavirus envelope: homotypic interactions between the M proteins. *J Virol* **74**, 4967-4978 (2000).
70. D. C. Dinesh *et al.*, Structural basis of RNA recognition by the SARS-CoV-2 nucleocapsid phosphoprotein. *PLoS Pathog* **16**, e1009100 (2020).
71. K. M. Scherer *et al.*, SARS-CoV-2 nucleocapsid protein adheres to replication organelles before viral assembly at the Golgi/ERGIC and lysosome-mediated egress. *Sci Adv* **8**, eabl4895 (2022).
72. L. G. Thorne *et al.*, Evolution of enhanced innate immune evasion by SARS-CoV-2. *Nature* **602**, 487-495 (2022).
73. S. Leary *et al.*, Generation of a Novel SARS-CoV-2 Sub-genomic RNA Due to the R203K/G204R Variant in Nucleocapsid: Homologous Recombination has Potential to Change SARS-CoV-2 at Both Protein and RNA Level. *Pathog Immun* **6**, 27-49 (2021).
74. S. Lu *et al.*, The SARS-CoV-2 nucleocapsid phosphoprotein forms mutually exclusive condensates with RNA and the membrane-associated M protein. *Nature Communications* **12**, 502 (2021).
75. Z. Yang *et al.*, Engagement of the G3BP2-TRIM25 Interaction by Nucleocapsid Protein Suppresses the Type I Interferon Response in SARS-CoV-2-Infected Cells. *Vaccines (Basel)* **10** (2022).
76. G. M. Duke, A. C. Palmenberg, Cloning and synthesis of infectious cardiovirus RNAs containing short, discrete poly(C) tracts. *J Virol* **63**, 1822-1826 (1989).
77. K. J. Livak, T. D. Schmittgen, Analysis of relative gene expression data using real-time quantitative PCR and the 2(-Delta Delta C(T)) Method. *Methods* **25**, 402-408 (2001).

815 **LEGENDS**

816

817 **Fig. 1. SARS-CoV-2 N inhibits PKR-induced ISR, preventing translation arrest and SG**
818 **formation in HeLa and A549 cells.** (***A***) Schematic representation of the PKR-induced ISR
819 activation upon the pEGFP-N3 transfection in eukaryotic cells. Created with BioRender.com.
820 (***B***) HeLa and A549 cells were transfected with expression vector pEGFP-N3 (EGFP) or pEGFP-
821 N3 derivatives encoding SARS-CoV-2 N, MERS-4a, IAV-NS1 or Bw-CoV-AcP10 genetically
822 fused to EGFP. Induction of the ISR via dsRNA-mediated PKR activation or suppression
823 thereof was assessed by comparing EGFP fluorescence intensity and SG formation as
824 detected by immunofluorescence staining for G3BP2. (left panel) Transfected HeLa cells;
825 (immune)fluorescence microscopy images, representative results. Scale bars: 50 µm. (right
826 panel) Bar graphs for Hela and A549 cells showing the percentage of EGFP expressing cells
827 containing G3BP2-positive SGs. The results are representative of three independent
828 experiments counting >200 cells per sample. Standard deviation indicated by error bars; ***
829 p=0.001, **** p< 0.001, ns = not significant (one-way ANOVA with Dunnett post hoc test).
830 (***C***) HeLa PKR^{KO} cells were transfected as in B. Representative (immuno)fluorescence
831 microscopy images are shown. (***D***) Western-blot analysis for PKR, phosphorylated PKR (p-
832 PKR), GFP-fused proteins and β-actin. HeLa wt and PKR^{KO} cells, mock-transfected or
833 transfected with indicated plasmid were lysed at 24 hr. Of note, the larger yield of EGFP
834 versus EGFP-N is counter intuitive but can be explained from the fact that (i) this is an
835 ensemble measurement (for the total transfected cell population) versus the analysis of
836 individual cells by fluorescence microscopy and (ii) basal expression levels of the codon
837 optimized EGFP *prior* to ISR activation will exceed those the EGFP-N fusion protein, which is
838 non-codon optimized and three times larger in size (see also Fig. S2). (***E***) Inhibition of SG
839 formation and translational arrest by pEGFP-N3-expressed N proteins of MERS-CoV and
840 HCoV-229E. (Immuno)fluorescence analysis (left panel), quantitative representation of the
841 results and statistical analysis as in B.

842

843 **Fig. 2. Nucleocapsid domain N2b suppresses translational arrest and SG formation.** (***A***)
844 Schematic representation of truncated derivatives of SARS-CoV-2 N protein fused to EGFP
845 (left panel). The proteins were overexpressed from pEGFP-N3-based vectors in HeLa cells
846 and percentages of SG-positive cells were determined as in Fig. 1A (right panel). The data are

847 representative of three independent experiments with more than 200 cells counted for the
848 presence of G3BP2-positive SGs per individual sample. Standard deviation indicated by error
849 bars. For a statistical analysis of the results, see Table S1. (***B***) Representative results from
850 (immuno)fluorescence analysis of HeLa cells transfected to express the SARS-CoV-2 N
851 protein derivatives. Scale bar: 50 µm.
852
853 **Fig. 3. N2b mutations that disrupt dsRNA binding abrogate suppression of translational**
854 **arrest and SG formation.** (***A***) (left panel) Cartoon representation of the SARS-CoV-2 N2b
855 dimer (PDB ID code 7C22 (58); generated with PYMOL with monomers in grey and orange.
856 Top view displaying the positively charged central RNA-binding groove. Side chains of
857 Lys^{257} and Lys^{261}, shown for both monomers and marked for one, in sticks and colored by
858 element with carbon atoms in magenta. (right panel) Electrophoretic mobility shift assay
859 (EMSA) with bacterially expressed N2b and single (ss) and double-stranded (ds) RNA
860 oligonucleotides, designed after SARS-CoV-2 stem-loop II motif (s2m). Assays were
861 performed with N2b in 10- or 20-fold molar excess. Non-bound RNA was included as a
862 control (np, no protein). (***B***) The effect of N2b amino acid substitutions on binding of s2m
863 dsRNA (left) or a scrambled version thereof (right). EMSAs performed with N2b and mutant
864 derivatives in 20-fold molar excess. (***C***-***D***) Mutational analysis of SARS-CoV-2 N2b, full-length
865 SARS-CoV-2 N and full-length HCoV-229E N. Select surface-exposed charged residues were
866 substituted by Ala either individually or in combination as indicated and the effect on IRS-
867 induced translational arrest (C) and SG formation (D) was analyzed in HeLa cells as in Fig. 1.
868 For a statistical analysis of the results, see Table S2.
869
870 **Fig. 4. N-mediated suppression of SG formation and ISR-induced translational arrest is not**
871 **affected by posttranslational modifications or G3BP1 interaction.** (***A***) The effect on N-
872 mediated ISR inhibition by mutations introduced to prevent posttranslational modifications
873 ($K^{375}Q$, $K^{375}R$, $R^{95}K$), to disrupt the G3BP1/2 binding site (1A-4A mutants) or to prevent
874 phosphorylation of the SR element (13S>A) was tested in HeLa cells by
875 (immune)fluorescence analysis as in Fig. 1. Scale bar: 50 µm. (***B***). Quantification of the
876 results in (A) representative of three independent experiments, with >200 cells counted per
877 sample as in Fig. 1. (***C***) Pull down assay to test SARS-CoV-2 N mutants for their association
878 with endogenous G3BP1 in HeLa wt (left panel) and PKR^{KO} cells (right panel).

879

880 **Fig. 5. The effect of N-G3BP interaction on arsenite-induced SGs in HeLa PKR^{KO} cells.**
881 HeLa PKR^{KO} cells were transfected to express EGFP, SARS-CoV-2 N wt, N mutants defective in
882 G3BP binding (1A-4A mut), N-K^{257}A+K^{261}A (N2b mut) or a mutant 'N1a + N2b mut' with
883 substitutions in both the G3BP binding site (2A mut) and N2b (K^{257}A+K^{261}A). At 24 hrs post
884 transfection, cells were sodium arsenite-treated to induce HRI-mediated ISR with ensuing
885 formation of SGs. (***A***) Representative (immune)fluorescence images. Scale bar: 50 µm.
886 Quantification of the results based on three independent experiments (***B***) by counting all
887 cells with detectable EGFP fluorescence or (***C***) highly expressing cells exclusively. For a
888 statistical analysis of the results, see **Table S3**.

889

890 **Fig. 6. Quantitative assessment of N-mediated rescue of ISR-induced translational arrest.**
891 HeLa cells were transfected to express EGFP, SARS-CoV-2 N2b, the full-length N proteins of
892 SARS-CoV-2 and HCoV-229E, and mutants thereof from pEGFP-N3-based expression vectors
893 to induce PKR-activated ISR. The capacity of these proteins to rescue translational repression
894 of red fluorescent protein (RFP) *in trans* or lack thereof was measured by flow cytometry at
895 24 hr post transfection (left panels) and fluorescence microscopy (see **Fig. S4**).
896 Representative flow cytometry histograms shown. The transfected cells were divided into
897 non-RFP-expressing, low (L) RFP-expressing and high (H) RFP-expressing populations (see
898 dashed lines in histograms). For each mutant protein, the [H/L] ratio was calculated and
899 normalized, with those of the corresponding wildtype proteins set at 100%. The bar graphs
900 show mean values with standard deviations based on three independent experiments
901 (unpaired t-test; ****, P<0.001; ns, non-significant) (right).

902

903 **Fig. 7. The N2b domain inhibits PKR phosphorylation, prevents SG formation, and reduces**
904 **the type I interferon response in EMCV infected cells.** (***A***) Structure of the polyprotein of
905 recombinant EMCV-L^{zn}-N2aN2b. Schematic representation and a close-up of the N-terminal
906 region with mature cleavage products shown as boxes. Red asterisks indicate the locations
907 of mutations (C^{19}A/C^{22}A) in the Zn-finger domain of leader protein L, which abolish its
908 function as EMCV-autologous antagonist of the host innate immune response. The red
909 arrowhead indicates the location of a newly engineered EMCV 3C cleavage site. The yellow
910 box depicts the native N-terminus of the EMCV polyprotein, i.e. the six N-terminal residues

911 of L and two residues encoded by a synthetic *Xho*I cloning site (see **Fig. S5** for details). The
912 location of the introduced SARS-CoV-2 N2a2b element is given, with the N2b domain in blue
913 and a Strep2 tag in grey. (***B***) SG formation in EMCV-infected cells is prevented by SARS-CoV-2
914 N2a2b. HeLa cells were infected at MOI 10 with EMCV-L^{zn} recombinant viruses expressing
915 N2a2b or a derivative 'N2a2b-Mut' in which the N2b RNA binding site was abolished by
916 Lys^{257}Ala and Lys^{261}Ala substitutions. Cells infected with parental wildtype EMCV or EMCV-L^{zn}
917 served as controls as were cells infected with recombinant EMCV-L^{zn} derivatives encoding
918 established coronavirus ISR antagonists MERS 4a and BW-Acp10. Cells were fixed at 8 hpi
919 and analyzed by immunofluorescence staining for dsRNA as a marker for infection and for SG
920 scaffold protein G3BP2. (***C***) Percentages of infected cells with stress granules at 6 and 8 hpi.
921 Bar graphs show the means of three independent experiments with more than 200 infected
922 cells counted per sample. Standard deviations indicated by error bars; **** $p< 0.0001$, ns =
923 not significant (two-way ANOVA with Dunnett post hoc test). (***D***) Western-blot analysis for
924 PKR, phosphorylated PKR (p-PKR), EMCV capsid proteins and β-actin. HeLa cells, mock-
925 infected or infected with recombinant EMCVs at MOI 10, were lysed at 6 or 8 hpi. Images
926 shown are representative of three independent experiments. (***E***) Suppression of type I
927 interferon response in EMCV-infected cells by N2a2b but not N2aN2b-Mut. HeLa cells, mock
928 infected or infected at MOI 10 with the indicated recombinant EMCV-L^{zn} viruses, were lysed
929 at 6 or 8 hpi. Total RNA was isolated and used for RT-qPCR analysis for IFN-β and actin. The
930 IFN-β levels were calculated as fold induction compared to levels in mock-infected cells,
931 after correction for actin mRNA levels, and normalized with EMCV-L^{zn} IFN-β levels set at
932 100%. Data represent means of three independent experiments. Standard deviations
933 indicated by error bars; statistical significance compared to the results for EMCV-L^{zn} or
934 EMCV-L^{zn}-N2aN2b infected cells calculated by two-way ANOVA with the Dunnett post hoc
935 test; ** $p<0.01$; *** $p<0.001$; **** $p<0.0001$.
936
937
938

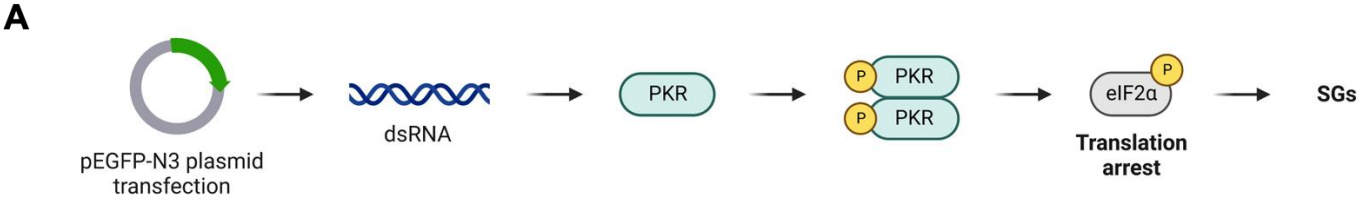
A
pEGFP-N3 plasmid transfection
dsRNA
PKR
P
PKR
P
PKR
eIF2α
P
Translation arrest
SGs

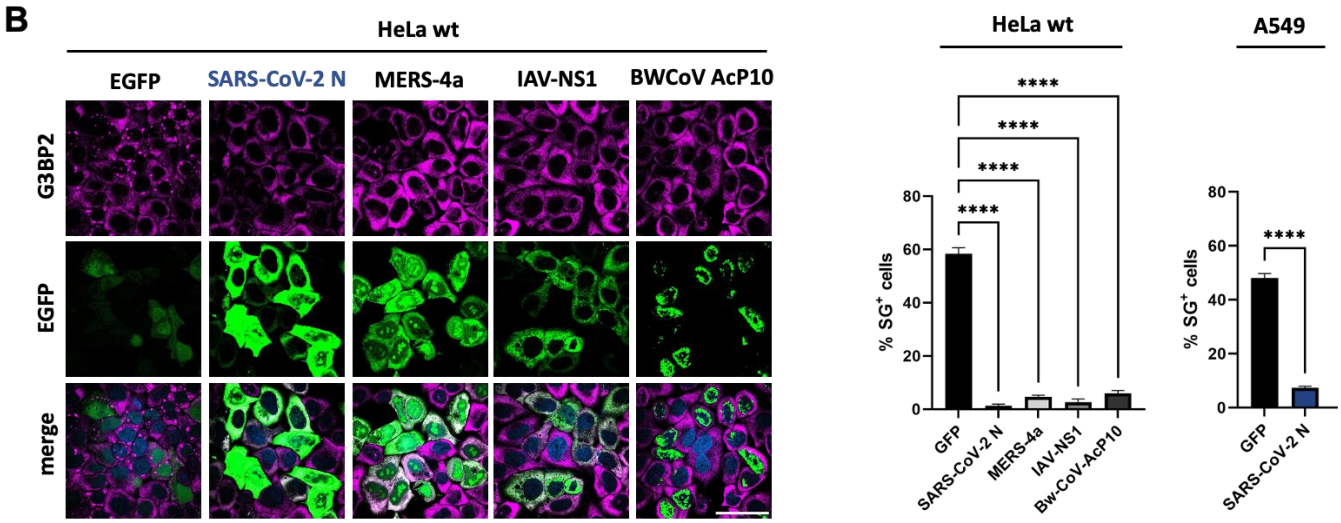
B
HeLa wt
EGFP
SARS-CoV-2 N
MERS-4a
IAV-NS1
BWCoV AcP10
G3BP2
EGFP
merge
HeLa wt
A549
% SG+ cells
GFP
SARS-CoV-2 N
MERS-4a
IAV-NS1
Bw-CoV-AcP10
****

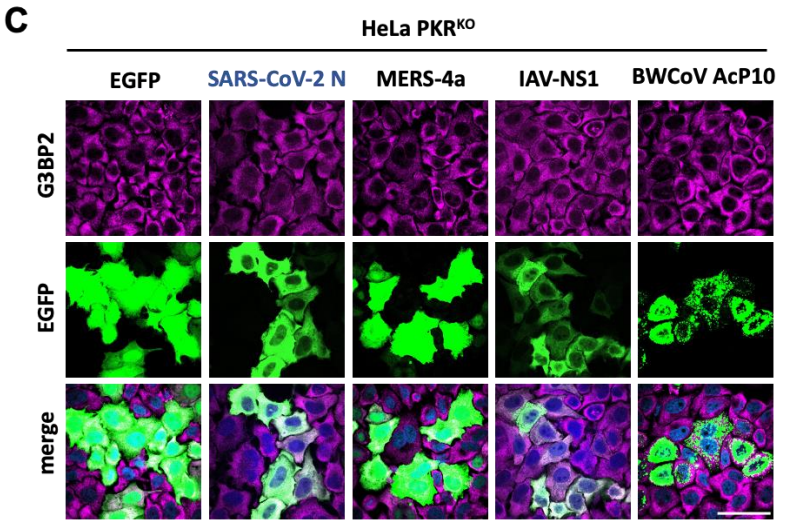
C
HeLa PKRKO
EGFP
SARS-CoV-2 N
MERS-4a
IAV-NS1
BWCoV AcP10
G3BP2
EGFP
merge

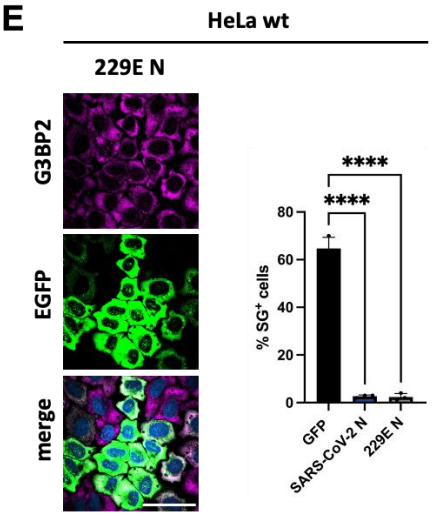
E
HeLa wt
229E N
G3BP2
EGFP
merge
% SG+ cells
GFP
SARS-CoV-2 N
229E N
****

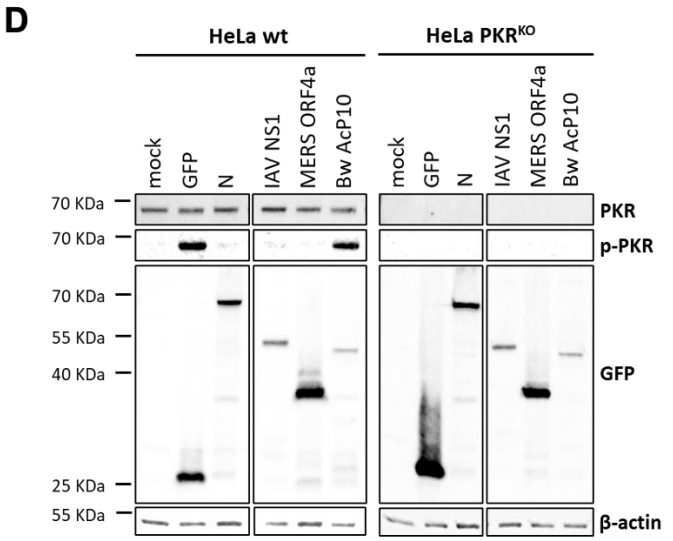
D
HeLa wt
HeLa PKRKO
mock
GFP
N
IAV NS1
MERS ORF4a
Bw AcP10
70 KDa
55 KDa
40 KDa
25 KDa
PKR
p-PKR
GFP
β-actin

Fig. 1

A

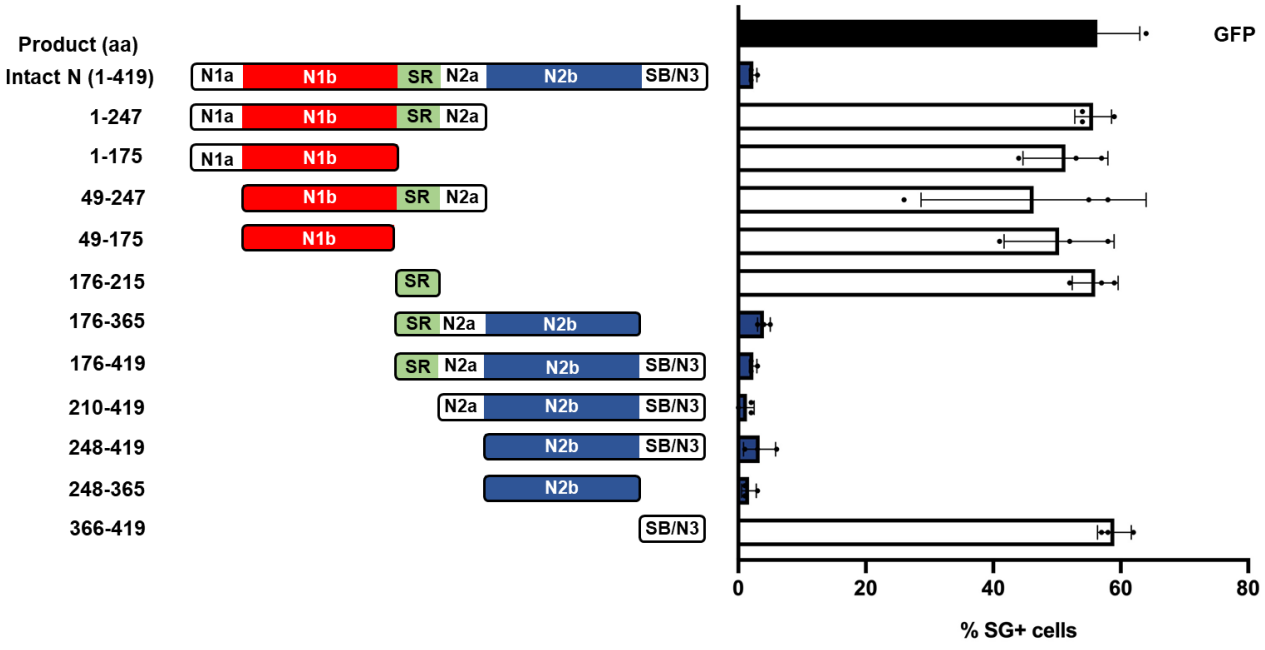
Product (aa)
Intact N (1-419)
1-247
1-175
49-247
49-175
176-215
176-365
176-419
210-419
248-419
248-365
366-419
N1a
N1b
SR
N2a
N2b
SB/N3
GFP
0
20
40
60
80
% SG+ cells

B

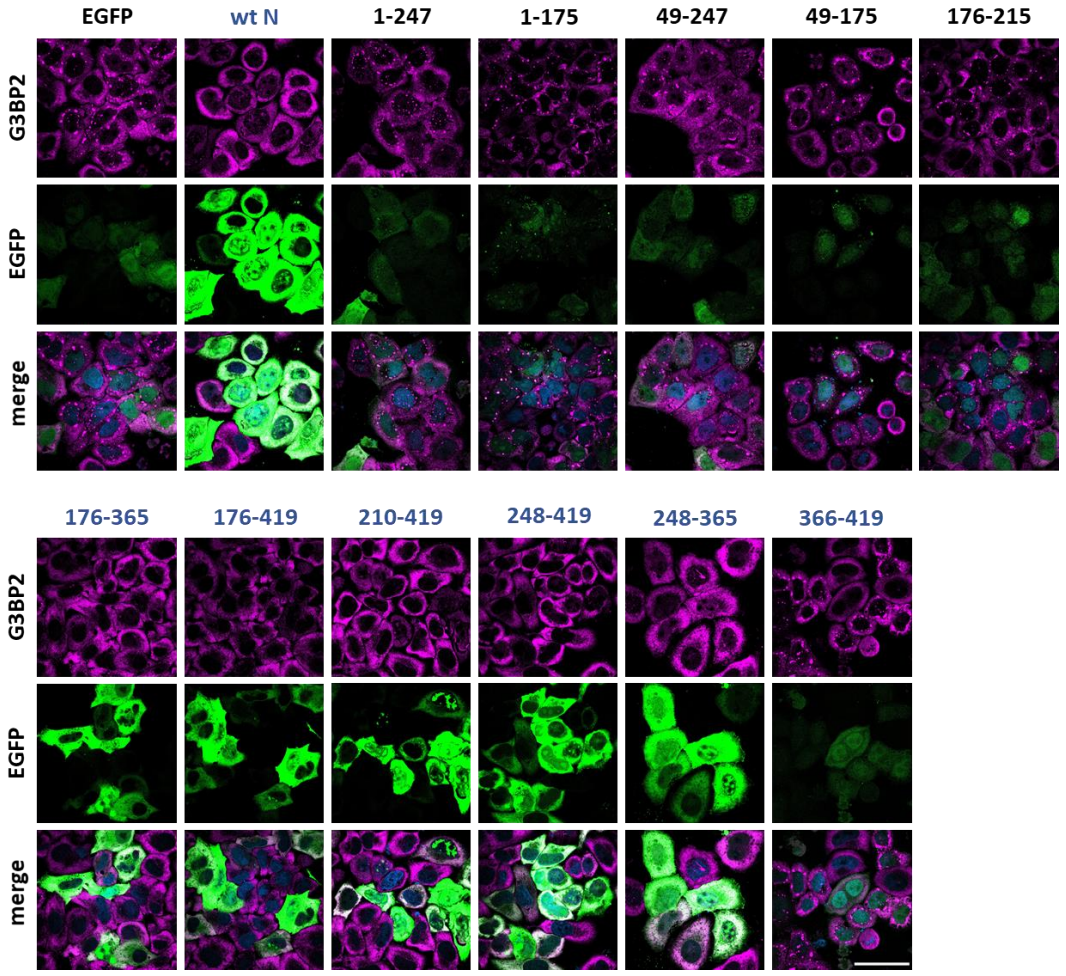
EGFP
wt N
1-247
1-175
49-247
49-175
176-215
176-365
176-419
210-419
248-419
248-365
366-419
G3BP2
EGFP
merge

Fig.2

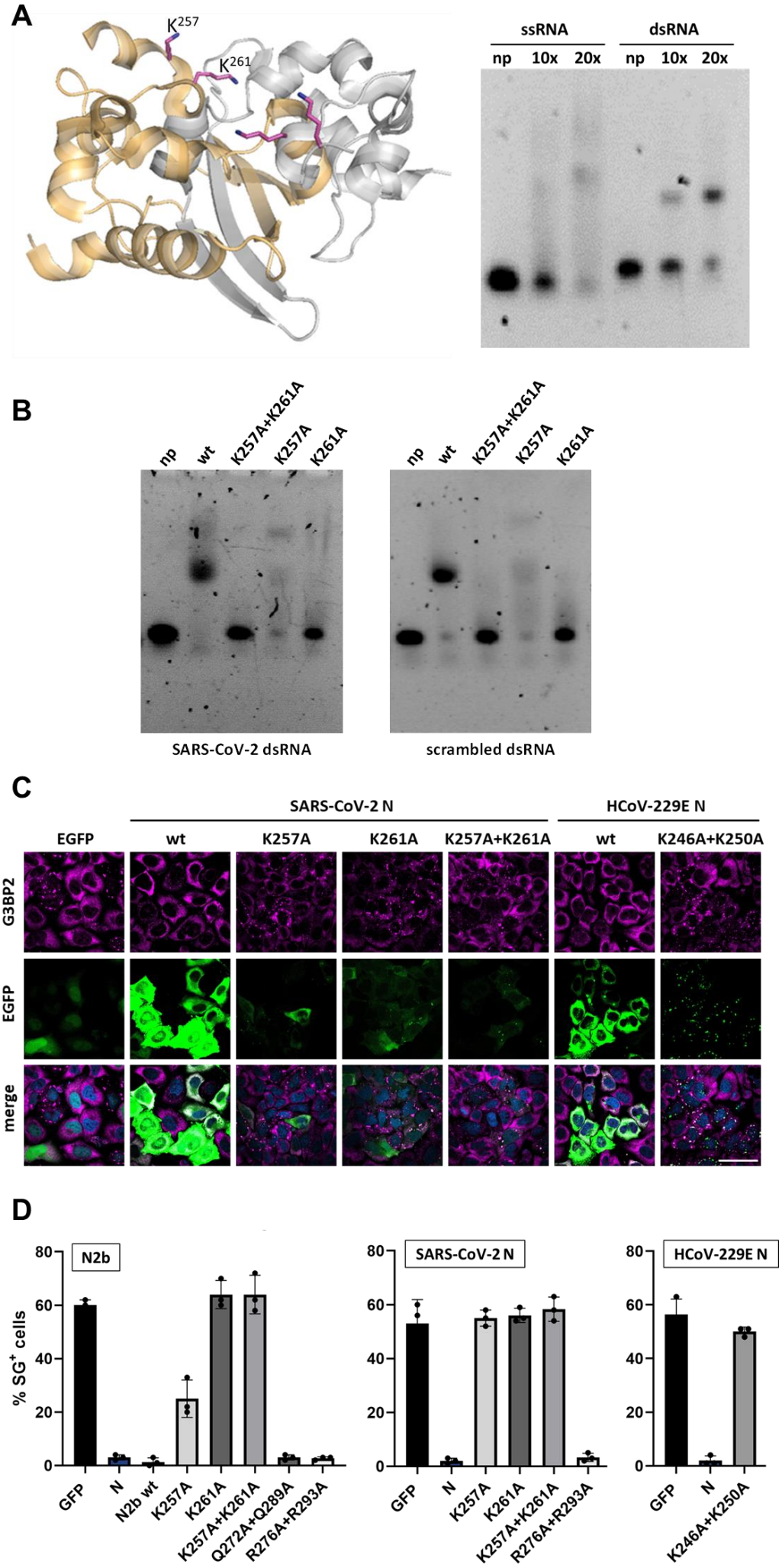
A
K257
K261
ssRNA
dsRNA
np
10x
20x
np
10x
20x
B
np
wt
K257A+K261A
K257A
K261A
np
wt
K257A+K261A
K257A
K261A
SARS-CoV-2 dsRNA
scrambled dsRNA
C
SARS-CoV-2 N
HCoV-229E N
EGFP
wt
K257A
K261A
K257A+K261A
wt
K246A+K250A
G3BP2
EGFP
merge
D
N2b
SARS-CoV-2 N
HCoV-229E N
% SG+ cells
0
20
40
60
80
GFP
N
N2b wt
K257A
K261A
K257A+K261A
Q272A+Q289A
R276A+R293A
K246A+K250A

Fig.3

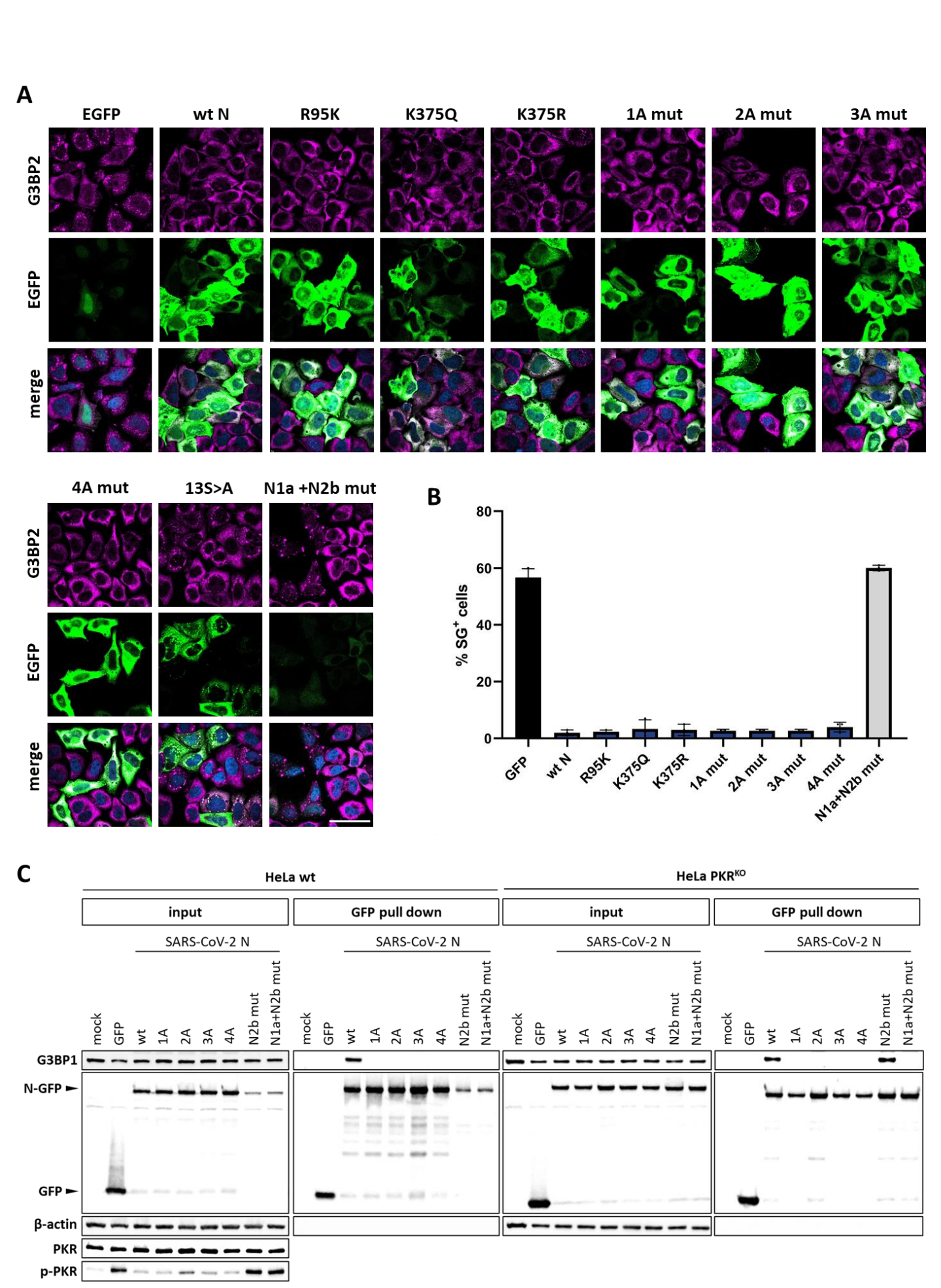
A
EGFP
wt N
R95K
K375Q
K375R
1A mut
2A mut
3A mut
4A mut
13S>A
N1a +N2b mut
G3BP2
EGFP
merge
B
% SG+ cells
80
60
40
20
0
GFP
wt N
R95K
K375Q
K375R
1A mut
2A mut
3A mut
4A mut
N1a+N2b mut
C
HeLa wt
HeLa PKRKO
input
GFP pull down
SARS-CoV-2 N
mock
GFP
wt
1A
2A
3A
4A
N2b mut
N1a+N2b mut
G3BP1
N-GFP
GFP
β-actin
PKR
p-PKR

Fig.4

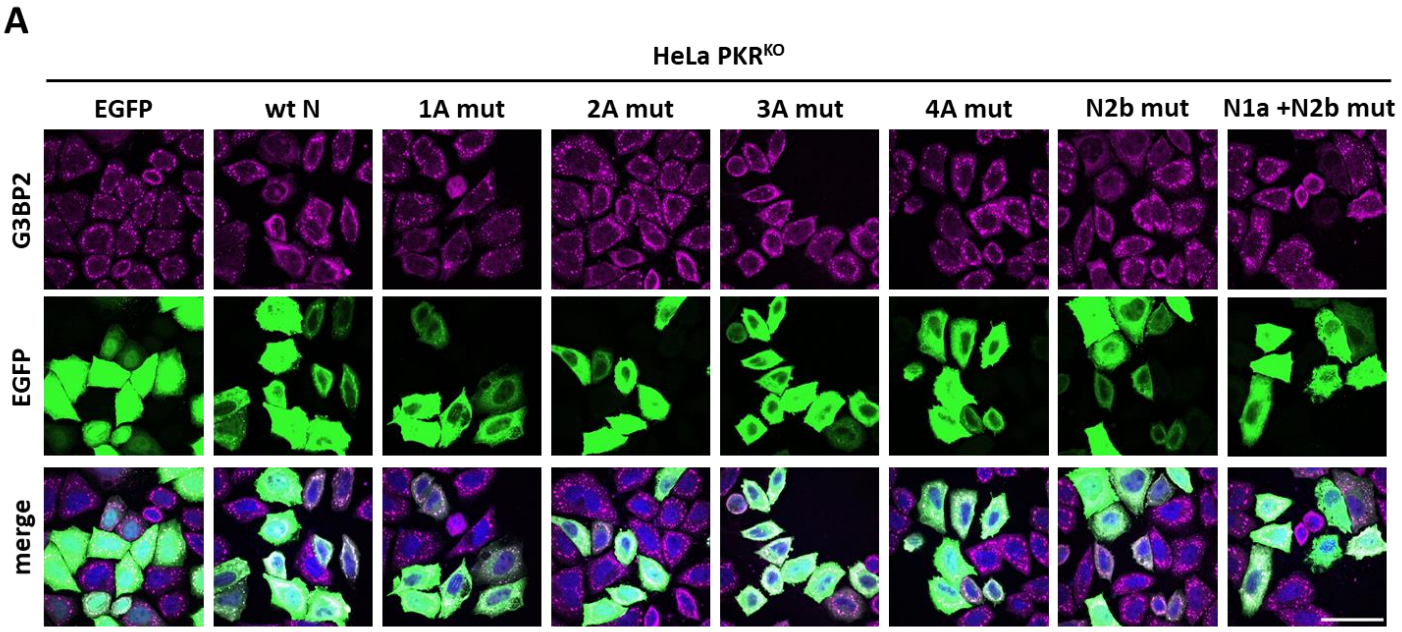
A
HeLa PKR^KO
EGFP
wt N
1A mut
2A mut
3A mut
4A mut
N2b mut
N1a +N2b mut
G3BP2
EGFP
merge

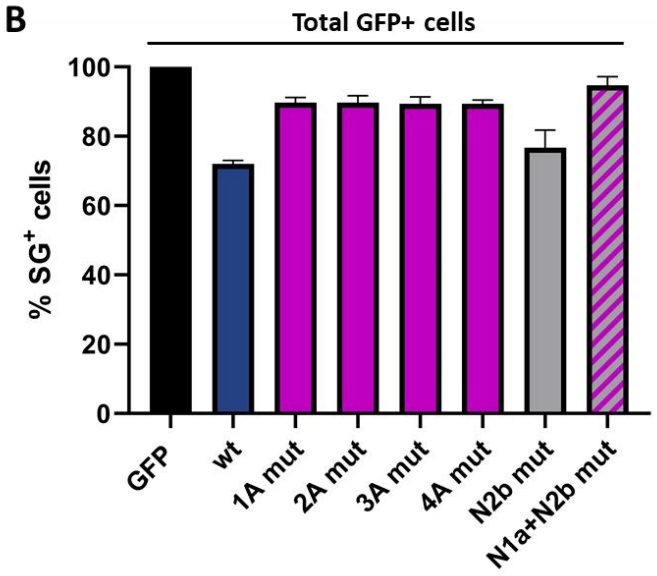
B
Total GFP+ cells
% SG+ cells
100
80
60
40
20
0
GFP
wt
1A mut
2A mut
3A mut
4A mut
N2b mut
N1a+N2b mut

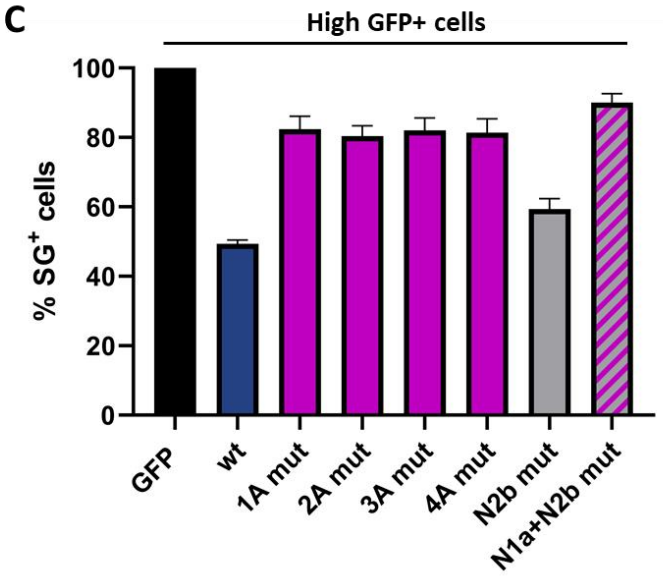
C
High GFP+ cells
% SG+ cells
100
80
60
40
20
0
GFP
wt
1A mut
2A mut
3A mut
4A mut
N2b mut
N1a+N2b mut

Fig.5

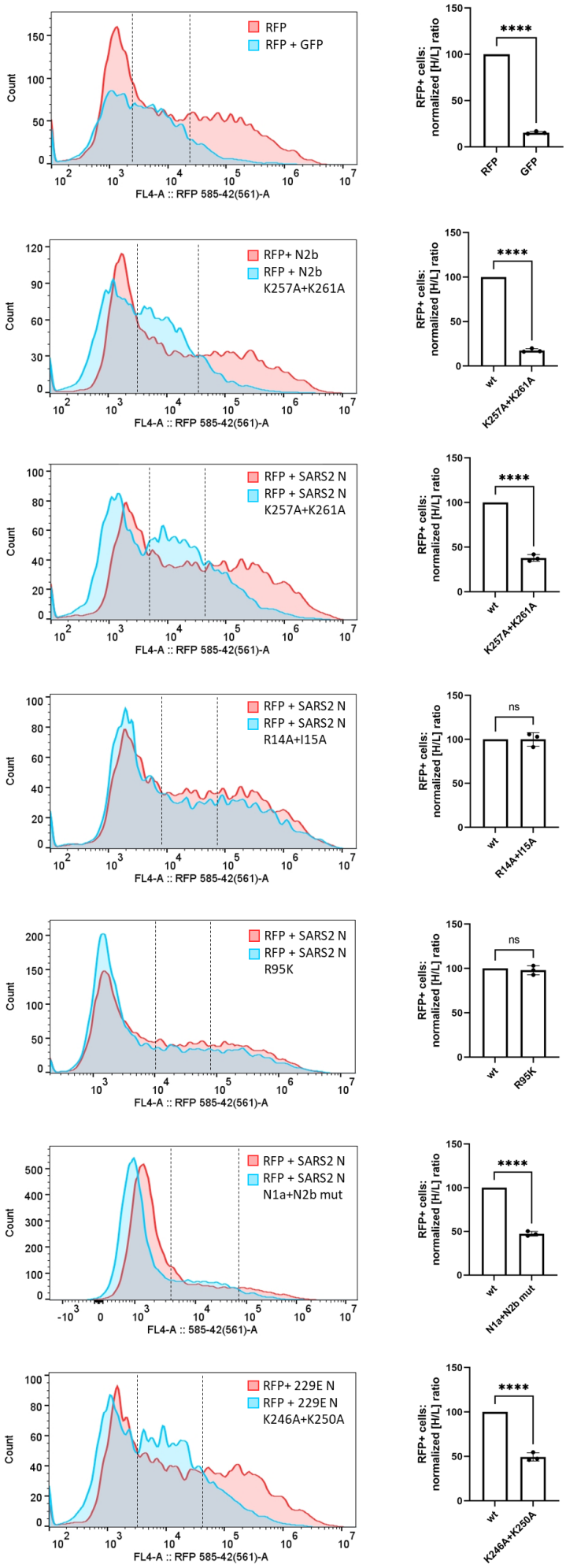
RFP
RFP + GFP
Count
FL4-A :: RFP 585-42(561)-A
RFP+ cells: normalized [H/L] ratio
****
RFP
GFP
RFP+ N2b
RFP + N2b K257A+K261A
wt
K257A+K261A
RFP + SARS2 N
RFP + SARS2 N K257A+K261A
RFP + SARS2 N
RFP + SARS2 N R14A+I15A
ns
R14A+I15A
RFP + SARS2 N
RFP + SARS2 N R95K
R95K
RFP + SARS2 N
RFP + SARS2 N N1a+N2b mut
N1a+N2b mut
RFP+ 229E N
RFP + 229E N K246A+K250A
K246A+K250A

Fig.6

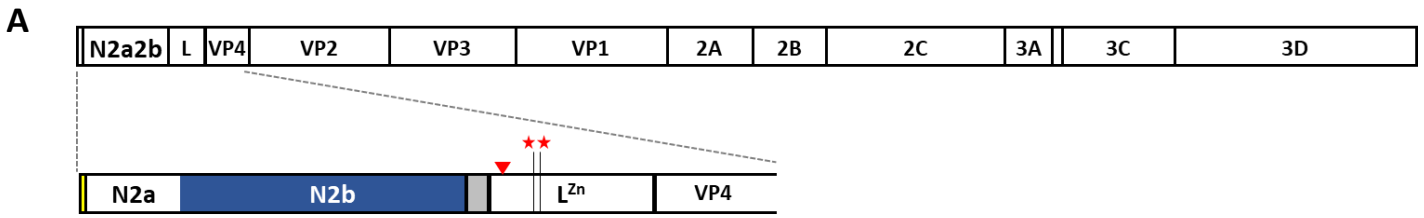
A
N2a2b
L
VP4
VP2
VP3
VP1
2A
2B
2C
3A
3C
3D
N2a
N2b
L^Zn
VP4

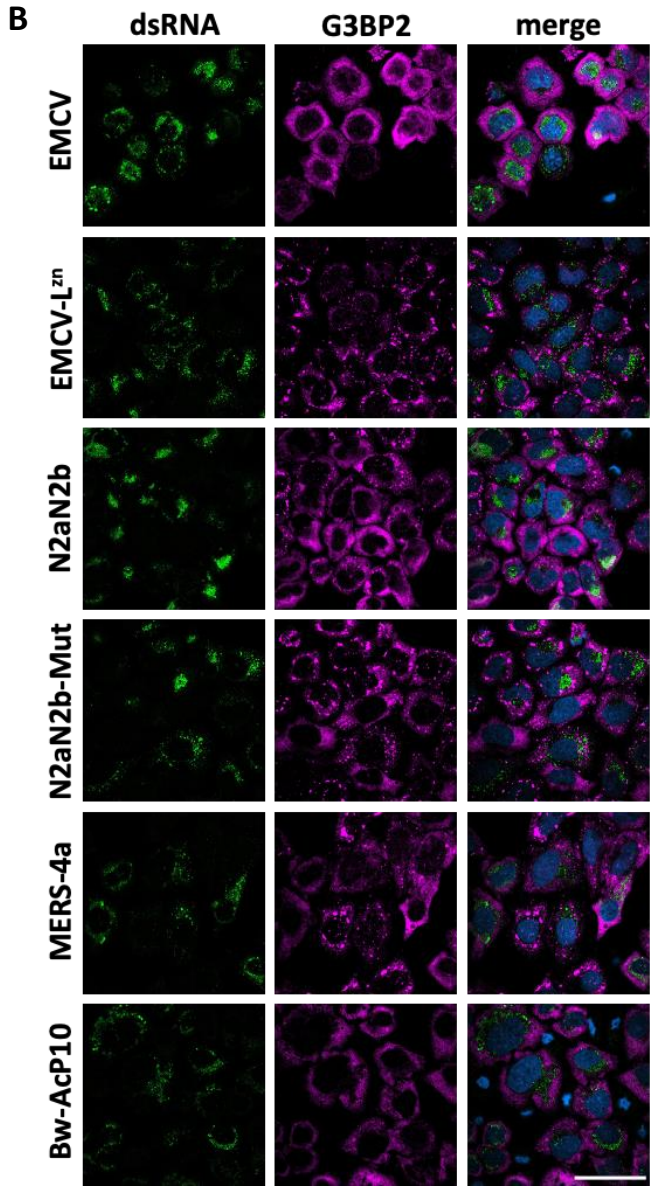
B
dsRNA
G3BP2
merge
EMCV
EMCV-L^zn
N2aN2b
N2aN2b-Mut
MERS-4a
Bw-AcP10

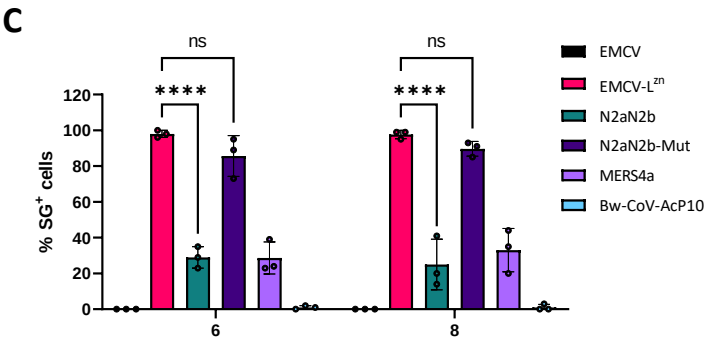
C
ns
****
ns
****
% SG+ cells
120
100
80
60
40
20
0
6
8
EMCV
EMCV-L^zn
N2aN2b
N2aN2b-Mut
MERS4a
Bw-CoV-AcP10

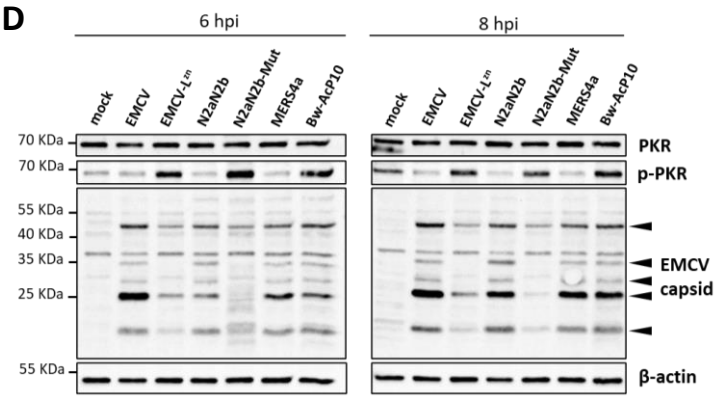
D
6 hpi
8 hpi
mock
EMCV
EMCV-L^zn
N2aN2b
N2aN2b-Mut
MERS4a
Bw-AcP10
70 KDa
70 KDa
55 KDa
40 KDa
35 KDa
25 KDa
55 KDa
PKR
p-PKR
EMCV capsid
β-actin

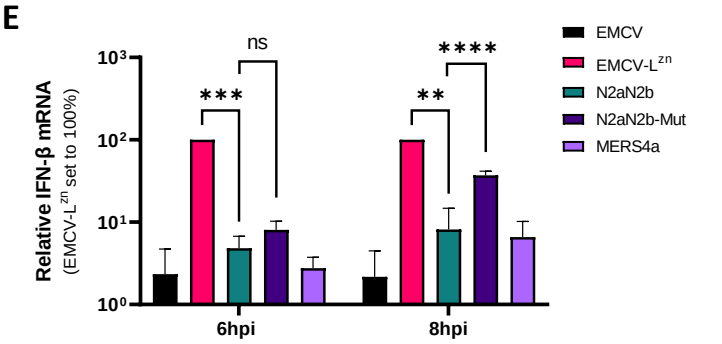
E
Relative IFN-β mRNA
(EMCV-L^zn set to 100%)
10^3
10^2
10^1
10^0
***
ns
**
****
6hpi
8hpi
EMCV
EMCV-L^zn
N2aN2b
N2aN2b-Mut
MERS4a

Fig.7